

THE KINEMATICS OF C IV IN STAR-FORMING GALAXIES AT $Z \sim 1.2$ XINNAN DU (杜辛楠)¹, ALICE E. SHAPLEY¹, CRYSTAL L. MARTIN², ALISON L. COIL³*Draft Version September 4, 2018*

ABSTRACT

We present the first statistical sample of rest-frame far-UV spectra of star-forming galaxies at $z \sim 1$. These spectra are unique in that they cover the high-ionization C IV $\lambda\lambda 1548, 1550$ doublet. We also detect low-ionization features such as Si II $\lambda 1527$, Fe II $\lambda 1608$, Al II $\lambda 1670$, Ni II $\lambda\lambda 1741, 1751$ and Si II $\lambda 1808$, and intermediate-ionization features from Al III $\lambda\lambda 1854, 1862$. Comparing the properties of absorption lines of lower- and higher- ionization states provides a window into the multi-phase nature of circumgalactic gas. Our sample is drawn from the DEEP2 survey and spans the redshift range $1.01 \leq z \leq 1.35$ ($\langle z \rangle = 1.25$). By isolating the interstellar C IV absorption from the stellar P-Cygni wind profile we find that 69% of the C IV profiles are blueshifted with respect to the systemic velocity. Furthermore, C IV shows a small but significant blueshift relative to Fe II (offset of the best-fit linear regression $-76 \pm 26 \text{ km s}^{-1}$). At the same time, the C IV blueshift is on average comparable to that of Mg II $\lambda\lambda 2796, 2803$. At this point, in explaining the larger blueshift of C IV absorption at the ~ 3 -sigma level, we cannot distinguish between the faster motion of highly-ionized gas relative to gas traced by Fe II, and filling in on the red side from resonant C IV emission. We investigate how far-UV interstellar absorption kinematics correlate with other galaxy properties using stacked spectra. These stacking results show a direct link between C IV absorption and the current SFR, though we only observe small velocity differences among different ionization states tracing the outflowing ISM.

Subject headings: galaxies: evolution – ISM: structure – ultraviolet: galaxies

1. INTRODUCTION

Outflows play a key role in the evolution of galaxies. Along with inflows, they regulate the amount of gas available for star formation, and remove metals from galaxies, polluting the intergalactic medium (IGM). These galactic-scale outflows have high velocities, typically several hundreds km s^{-1} , and high mass loss rates, commonly ranging from a few tenths up to the same order as the SFR (e.g., Heckman et al. 2000; Pettini et al. 2001; Shapley et al. 2003; Martin 2005; Weiner et al. 2009; Steidel et al. 2010). Galactic winds may either be driven by thermal pressure associated with the supernova explosions, or else radiation pressure on dust grains from absorption and scattering of continuum photons emitted by massive stars (Murray et al. 2005).

Galactic winds appear to be ubiquitous in galaxies with star-formation surface densities above a given threshold (Heckman et al. 2001), ranging from dwarf galaxies (Martin 1999; Heckman et al. 2001; Schwartz & Martin 2004) to Ultra Luminous Infrared Galaxies (ULIRGs; Martin 2005; Martin & Bouché 2009), and are especially common at high redshift (e.g., Pettini et al. 2002; Shapley et al. 2003; Weiner et al. 2009). Outflows have typically been probed with narrowband imaging (for example, H α) and spectra of metal absorption lines. Unsaturated lines can be used to infer the ionic column density, which can potentially provides estimates of the mass and metallicity of outflowing material. Saturated lines are still useful for probing outflow kinematics.

Outflows have a complex multi-phase structure, which

can be probed using neutral, low- and high-ionization absorption features. Most studies of outflows have focused on low-ionization absorption lines, although there are observations of high-ionization lines for a small number of individual galaxies and from specific examples of composite spectra, (e.g., Heckman et al. 2001; Shapley et al. 2003; Schwartz et al. 2006; Grimes et al. 2009). It is not clear how the kinematics of high-ionization features relate in general to those of low-ionization lines. Some results show that the high-ionization absorption lines have a larger blueshift than the low-ionization lines by studying the coronal-phase O VI (e.g. Heckman et al. 2001; Grimes et al. 2009) and C IV (Wolfe & Prochaska 2000), while others claim that there is no significant difference between the kinematics of high- and low-ionization lines (Pettini et al. 2002; Shapley et al. 2003; Chisholm et al. 2016). In order to gain a robust handle on the overall mass outflow rate in galactic winds, it is important, however, to understand their detailed multi-phase structure, and compare the properties of different phases of the outflow. Despite the challenges associated with using C IV as a tracer of galactic outflows, mainly because of the superposition of stellar and interstellar C IV absorption and emission, this resonant transition potentially provides a very useful probe of the warm and hot phases of outflowing interstellar gas (e.g. Heckman et al. 2001; Shapley et al. 2003; Schwartz et al. 2006; Grimes et al. 2009).

Starburst-driven outflows were first studied in the local universe (e.g., Heckman et al. 1990; Martin 1999) and at $z > 2$ (Shapley et al. 2003; Pettini et al. 2001; Steidel et al. 2004). Relatively recently, $z \sim 1$ has become a focus of gas outflow studies. Low-ionization lines (e.g., from Mg II and Fe II) are commonly used for probing the cool phase of $z \sim 1$ outflows (e.g. Weiner et al. 2009; Martin et al. 2012; Kornei et al.

¹ Department of Physics and Astronomy, University of California, Los Angeles CA, 90095, USA

² Department of Physics, University of California, Santa Barbara CA, 93106, USA

³ Department of Physics, University of California, Santa Diego CA, 92093, USA

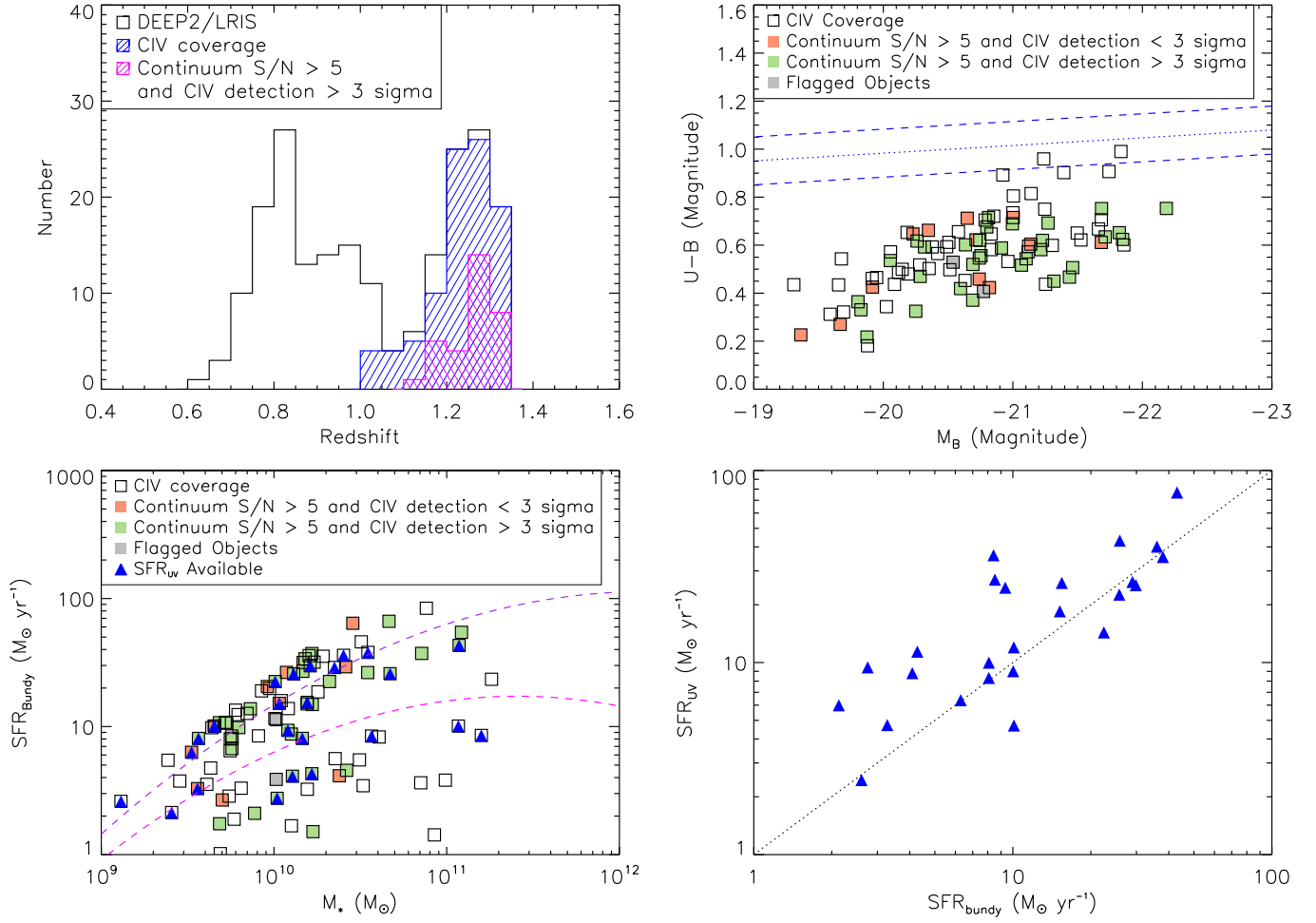


FIG. 1.— Properties of the galaxies in the DEEP2 C IV sample. **Top left:** Redshift distribution. The black open bar represents the parent sample of 208 DEEP2/LRIS galaxies; the dashed blue bar represents 93 galaxies with C IV coverage; The dashed magenta bar represents 32 galaxies meeting the criterion of continuum $S/N > 5$ and C IV detection $> 3\sigma$ ($EW/\delta EW > 3$). **Top right:** $U-B$ vs. M_B color-magnitude diagram. Squares represent 93 objects with C IV coverage; filled squares represent those with continuum $S/N > 5$; green squares denote galaxies with C IV $S/N > 3$ (32 objects) while orange squares denote those with C IV $S/N < 3$ (12 objects). gray squares represent galaxies showing asymmetric absorption on the red end of C IV (2 objects, see Section 3.1). The dotted line marks the division between the “red sequence” and the “blue cloud” at $z \sim 1$ in the DEEP2 sample (Willmer et al. 2006). **Bottom left:** Bundy SFR vs. stellar mass. Both stellar mass and Bundy SFR were derived from SED fitting assuming a Chabrier IMF. Color coding of the symbols is the same as in the top right panel. The blue filled triangles show where both Bundy SFR and SFR_{UV} are available. The pink and purple dashed lines denote the SFR - M_* relation for redshift ranges of $0.5 < z < 1.0$ and $1.0 < z < 1.5$, respectively (Whitaker et al. 2014). **Bottom right:** Comparison between Bundy SFR and SFR_{UV} for the subset of 25 objects in the AEGIS field with both types of measurements. SFR_{UV} was measured from the dust-corrected UV luminosity from GALEX (see the text in Section 2 for a full description) and has been converted to a Chabrier IMF. The black dotted line indicates a 1:1 relation.

2012, 2013; Rubin et al. 2014). Although outflows are much more commonly detected than inflows at this redshift, rare instances of infalling gas have also been discovered (Coil et al. 2011; Martin et al. 2012; Kornei et al. 2012; Rubin et al. 2014). In terms of outflow demographics, the outflow velocity traced by low-ionization lines is correlated with stellar mass, SFR and SFR surface density (Weiner et al. 2009; Kornei et al. 2012), and the strength of these lines increases with stellar mass, B -band luminosity, $U-B$ color and SFR (Martin et al. 2012; Rubin et al. 2014). Finally, in most star-forming galaxies at $z \leq 1.5$ outflows are inferred to have a bipolar geometry, as indicated by the detection fraction of blueshifted gas and extraplanar absorption (e.g. Rupke et al. 2005; Martin et al. 2012; Bordoloi et al. 2014; Rubin et al. 2014) and the fact that

face-on galaxies tend to have a slightly faster outflow speed (Kornei et al. 2012).

In this study we focus on the high-ionization C IV $\lambda\lambda 1548, 1550$ doublet for the first time at $z \sim 1$. We also measure the kinematics of other far-UV low-ionization lines (Si II $\lambda 1526$, Fe II $\lambda 1608$ and Al II $\lambda 1670$) and compare them with motions traced by near-UV Fe II and Mg II lines. Both observations and simulations have shown that C IV appears to trace two distinct types of gas: the hot ($T > 10^5$ K), denser, collisionally ionized gas in the coronal phase also probed by O VI absorption, and the warm ($T < 10^5$ K), less dense, photoionized gas that may be comoving with the gas the low-ionization lines trace (Lehner et al. 2011; Shen et al. 2013). Given the intermediate ionization stage of C IV relative to that of O VI and the low-ionization lines, it is essential to ex-

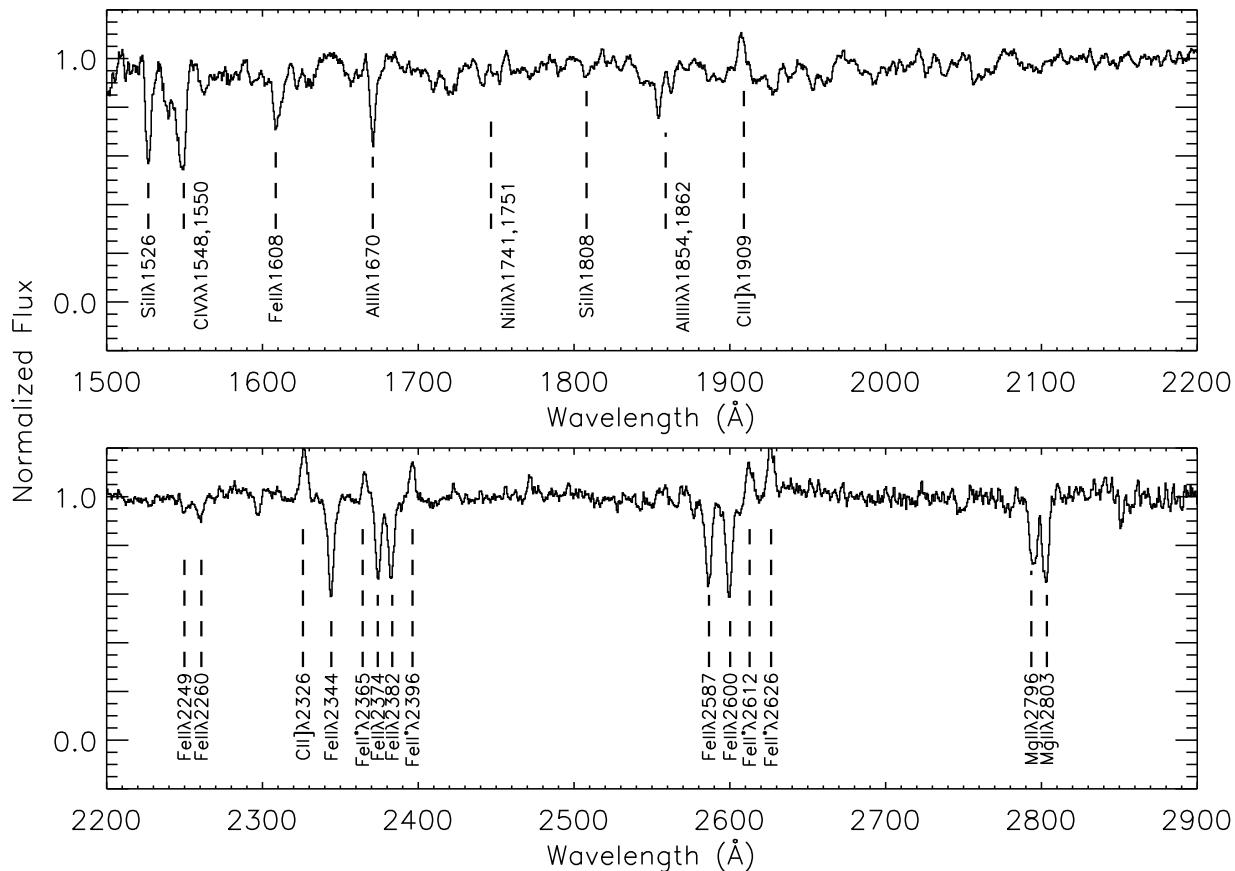


FIG. 2.— Composite continuum-normalized UV spectrum constructed from 93 objects with C IV coverage from the DEEP2/LRIS sample. Both strong and weak absorption features are identified. At the resolution of the LRIS spectra included in this composite, the C IV doublet is blended.

amine how its kinematics differ from those inferred from low-ionization lines. Comparing the properties of different ionization phases will provide us a better understanding of the multi-phase structure of gas flows.

We provide a brief overview of the observations and data reduction, and describe the selection criteria of our C IV sample in Section 2. In Section 3, we describe the measurements of gas kinematics traced by C IV and by other low-ionization lines. We compare the kinematics of C IV and the far-UV low-ionization lines with those of the near-UV Fe II and Mg II lines in Section 4, and present scaling relations between outflows and galaxy properties in Section 5. Finally, we summarize and discuss our results in Section 6.

Throughout this paper, we use a standard Λ -CDM model with $\Omega_m = 0.3$, $\Omega_\Lambda = 0.7$ and $H_0 = 70 \text{ km s}^{-1}$. All wavelengths are measured in vacuum. Magnitudes and colors are on the Vega system.

2. OBSERVATIONS, DATA REDUCTION AND SAMPLE

As described in Martin et al. (2012), our sample was drawn from the Deep Extragalactic Evolutionary Probe 2 (DEEP2; Newman et al. 2013) galaxy redshift survey and observed with the dichroic Low Resolution Imager and Spectrometer (LRIS, Oke et al. 1995; Steidel et al.

2004) on the Keck I telescope. The LRIS observations were conducted over the course of 4 observing runs from 2007 to 2009. Data were collected for 9 multi-object slit-masks using $1.2''$ slits. 208 galaxies were targeted based on apparent magnitude $B < 24.5$ varying in redshift from $z = 0.4 - 1.4$ with $\langle z \rangle = 1.01$. Two sets of masks were developed for the DEEP2/LRIS sample: one set (6 masks) was observed with the 400 lines mm^{-1} grism on the blue side with the average effective resolution of 435 km s^{-1} full width at half-maximum (FWHM), and the 831 lines mm^{-1} grating on the red side with FWHM of 150 km s^{-1} ($R = 700$). The other set (3 masks) was observed with the 600 lines mm^{-1} grism on the blue side with FWHM of 282 km s^{-1} , and the 600 lines mm^{-1} red grating with FWHM of 220 km s^{-1} ($R = 1100$). The integration time for most 400-line masks ranges from 5 to 9 hours. Galaxies at $1.19 \leq z \leq 1.35$ were prioritized on these masks, as the C IV $\lambda\lambda 1548, 1550$ doublet fell in a region of decent sensitivity ($\lambda \geq 3400 \text{ \AA}$). The 600-line grism masks were mainly designed for less optimal observing conditions in order to obtain the near-UV spectroscopy of brighter galaxies, with typically shorter total exposure time (3-5 hours). For objects observed with the 400-line masks, the blue side of the spectra were

designed to contain rest-UV interstellar absorption lines, with the red side covering the [O II] emission doublet. The 600-line spectra were typically designed for continuous wavelength coverage between the blue and red sides.

The data were reduced as described in Martin et al. (2012). In brief, the two-dimensional (2D) spectra were first flat fielded, cleaned of cosmic rays and background-subtracted. Individual 2D exposures were then combined, and extracted into one dimension (1D), and wavelength and flux calibrated. In most cases, the systemic redshift of each galaxy was determined from the [O II] doublet, which typically fell on the red side of the LRIS spectrum. For galaxies with no [O II] coverage in the LRIS spectra, the DEEP2 Keck/DEIMOS redshift was adopted. As discussed in Martin et al. (2012), we detect no systematic differences on average between the DEEP2 and LRIS [O II] systemic redshifts, for the 167 galaxies with both redshift measurements.

Rest-frame B -band luminosities and $U-B$ colors were taken from Willmer et al. (2006), and the stellar mass was derived from SED fitting with *BRICK* photometry, assuming a Chabrier (2003) initial mass function (IMF) and Bruzual & Charlot (2003) spectral templates (see Bundy et al. (2006) for a full description). Two types of SFR are shown in Figure 1: the one from Bundy et al. (2006) was estimated from SED fitting assuming a Chabrier IMF, while SFR_{UV} was derived from *Galaxy Evolution Explorer* (GALEX) measurements and corrected for dust attenuation. GALEX far-UV and near-UV photometry, along with B -band observations were used to determine β , the spectral slope where the continuum flux is in the form $f_\lambda \propto \lambda^\beta$ over the rest-frame wavelength range of 1250 - 2500Å. The β/A_{UV} relationship from Seibert et al. (2005) was then used to estimate the UV attenuation and thus to correct GALEX luminosities. Given the relation from Salim et al. (2007), the dust-corrected UV SFR was then calculated assuming a Salpeter (1955) IMF and converted to a Chabrier IMF by dividing by a factor of 1.8. 25 out of 93 objects in our sample are in the AEGIS field, where both types of SFR measurements are available. Since the SED-based SFR has several limitations and possible biases (e.g., age-dust-metallicity degeneracy, systematic dependence on assumed star-formation history; Papovich et al. 2001), we only adopted SFR_{UV} for the analysis presented here, despite its restricted coverage to our sample.

One unique aspect of the DEEP2/LRIS sample is that we optimized our mask design to cover C IV and the far-UV spectral region at $z \sim 1$. With this approach, we obtained C IV coverage for 93 out of 208 objects. A composite rest-UV spectrum of these 93 objects is shown in Figure 2, with the strongest rest-UV interstellar features marked. Of the 93 galaxies with C IV coverage, 46 had continuum signal-to-noise ratio (S/N) > 5 in the vicinity of C IV from 1570Å to 1590Å, a region in which the continuum is free of line features. We adopted this S/N threshold to isolate objects with robust C IV absorption-line measurements or limits. These 46 objects comprise the main sample for analysis, and they are representative of the full sample of galaxies with C IV coverage in terms of stellar mass, SFR, B -band luminosity and $U-B$ color, except being slightly bluer than average at the brightest B -band absolute magnitudes (Figure 1). In the full sam-

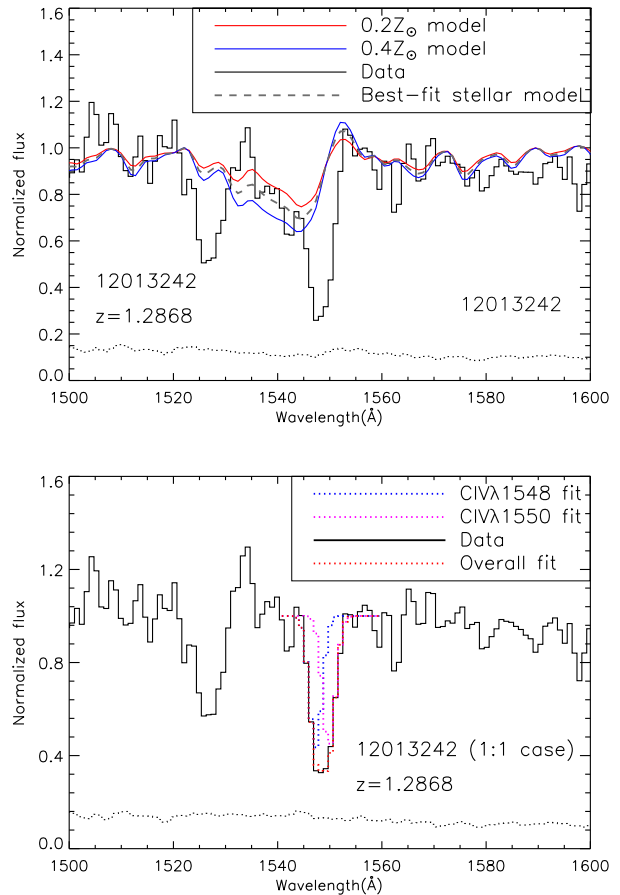


FIG. 3.— **Top:** Determination of the best-fit stellar model of object 12013242 (continuum $S/N = 16.4$). The red and blue lines indicate two stellar models ($0.2Z_\odot$ and $0.4Z_\odot$, with residuals 0.0624 and -0.0659, respectively) bracketing the P-Cygni absorption feature of C IV. The best-fit stellar model was calculated from a linear combination of these two models based on inverse residual weighting. The black dotted line represents the corresponding error spectrum of this object. **Bottom:** Deblending the interstellar C IV absorption trough into two Gaussian profiles. The fits for C IV λ1548 and C IV λ1550, respectively, are shown in blue and magenta dotted lines, and the overall fit is marked as the red dotted line. The centroid of the doublet members was fixed at the rest-wavelength ratio, and the EW of each member was assumed equal.

ple of 93 objects with C IV coverage, 81 were observed with the 400-line grism, and 12 with the 600-line grism. However, all but one object (ID: 32016683) in the high S/N sample were observed with the 600-line grism.

As illustrated in Figure 1, our sample with C IV coverage spans in redshift from 1.01 to 1.35 with a median of 1.25, B -band luminosities $-19.31 > M_B > -22.19$ with a median of -20.74, stellar mass $9.11 < \log(M_*/M_\odot) < 11.26$ with a median of 10.10, $U-B$ color from 0.18 to 0.99 with a median of 0.58 and SFR_{UV} from 2 to 77 $M_\odot \text{ yr}^{-1}$ with a median of 14 $M_\odot \text{ yr}^{-1}$. These galaxies primarily fall in the “blue cloud” (Faber et al. 2007) of star-forming galaxies at $z \sim 1$.

3. MEASUREMENTS

In this section, we describe the measurements of strong far-UV absorption features at wavelengths 1500Å to 1900Å, including the high-ionization dou-

blet C IV $\lambda\lambda 1548, 1550$, and low-ionization Si II $\lambda 1526$, Fe II $\lambda 1608$ and Al II $\lambda 1670$ features. We adopted single-component Gaussian fits as the simplest possible functional form to describe our absorption lines, as the data are not of sufficient resolution and S/N to consider more complicated models (especially for C IV, which already requires both stellar and interstellar model components).

3.1. Measurement of C IV

The C IV absorption profile is a complex superposition of stellar and interstellar components that needs to be disentangled in order to characterize the interstellar C IV absorption. The doublet members, C IV $\lambda 1548$ and C IV $\lambda 1550$, have a relative oscillator strength of 2:1. Therefore, the doublet ratio ranges from 2:1 in the optically thin case to 1:1 in the optically thick case. In this paper we adopted the saturated doublet ratio of 1:1 (yielding a rest-frame wavelength of 1549.5 Å for the blended C IV profile), based on the typical EW of the C IV feature in our sample (Pettini et al. 2002). Assuming the doublet ratio of 2:1 results in a velocity shift $\sim 84 \text{ km s}^{-1}$ less blueshifted than in the 1:1 case, although the optically-thin 2:1 ratio is unlikely to apply given the type of systems we probe.

We fit the rest-frame UV continuum in the 1D calibrated LRIS spectra using spectral regions (‘windows’) defined by Rix et al. (2004), which are clean of spectral features. We applied these ‘windows’ for fitting the continuum for all the spectra with the IRAF *continuum* routine, using a *spline3* function of order = 8. In cases where the fitted continuum level does not quite follow the observed spectrum due to the limited coverage of windows from Rix et al. (2004), we added additional windows, customized for each object, to keep the fitted continuum reasonable and make sure that the continuum scatters around unity.

The complexity of the observed C IV absorption profile stems from the joint contributions of stellar and interstellar components. The stellar part is the P-Cygni profile mainly produced by O and B stars, where the presence of blue shifted absorption and redshifted emission is the characteristic profile of a fast-moving stellar wind. In order to isolate the interstellar C IV absorption, we must normalize the continuum by the stellar P-Cygni profile. The spectral synthesis code of Leitherer et al. (2010) outputs the rest-frame UV spectra for stellar populations based on the assumption of constant star formation, a Salpeter IMF with mass limits of 1 and 100 M_{\odot} , and a range in metallicity including 0.05 Z_{\odot} , 0.2 Z_{\odot} , 0.4 Z_{\odot} , 1.0 Z_{\odot} and 2.0 Z_{\odot} . These spectra include the predicted stellar P-Cygni profiles based on models for the winds of hot stars from WM-Basic, which ranged in wavelength from 900 to 3000 Å at a resolution of 0.4 Å. We smoothed all 5 models to the resolution of our LRIS spectra (282 km s^{-1} FWHM or 1.4 Å at 1550 Å for 600-line masks, and 435 km s^{-1} FWHM or 2.2 Å at 1550 Å for 400-line masks) and continuum normalized them using the windows from Rix et al. (2004). For each stellar model we calculated the residual to the data based on inverse square weighting over the blue wing of C IV from 1535 Å to 1544 Å.

As shown in Equation 1, the residual, *res* is defined as:

$$res = \frac{\sum_i \frac{y_{model,i} - y_{data,i}}{y_{err,i}^2}}{\sum_i \frac{1}{y_{err,i}^2}} \quad (1)$$

where $y_{model,i}$, $y_{data,i}$ and $y_{err,i}$ are, respectively, the continuum-normalized stellar model from Leitherer et al. (2010), the science spectrum and the corresponding error spectrum at pixel i .

As presented in the top panel of Figure 3, we constructed a best-fit stellar model at each wavelength from the linear combination of the two models (red for 0.2 Z_{\odot} and blue for 0.4 Z_{\odot}) with P-Cygni absorption depths (i.e., metallicities) that bracketed the observed profile.

This best-fit model, *Bestfit*(λ), is characterized as:

$$\begin{aligned} Bestfit(\lambda) &= \frac{model_1(\lambda) \left| \frac{1}{res_1} \right| + model_2(\lambda) \left| \frac{1}{res_2} \right|}{\left| \frac{1}{res_1} \right| + \left| \frac{1}{res_2} \right|} \\ &= \frac{model_1(\lambda) |res_2| + model_2(\lambda) |res_1|}{|res_1| + |res_2|} \end{aligned} \quad (2)$$

where res_1 and res_2 are the residuals for *model*₁ (red), in the top panel of Figure 3 and *model*₂ (blue), respectively. As shown in Equation 2, the linear combination weights were determined from the inverse residual between model and data. In the top panel of Figure 3, the residuals for the 0.2 Z_{\odot} and 0.4 Z_{\odot} models are 0.0624 and -0.0659, respectively.

While bulk of the sample (93 objects with C IV coverage) is best described by models with 0.05 $Z_{\odot} < Z < 2.0Z_{\odot}$,⁴ 22 objects failed to be bracketed with neighboring metallicities, indicating that the C IV wing at 1535 Å to 1544 Å was either too shallow for the lowest metallicity or too deep for the highest. In such cases, we chose the best-fit to be either 0.05 Z_{\odot} (18 objects) or 2.0 Z_{\odot} (4 objects) for objects with, respectively, the shallowest and deepest stellar C IV absorption. We then divided both the continuum-normalized spectra and the error spectra by the corresponding best-fit stellar models and, accordingly, isolated the interstellar C IV absorption component.

Since the C IV $\lambda\lambda 1548, 1550$ doublet was not resolved in these low resolution spectra, we deblended the interstellar C IV profile into two Gaussian profiles for the 46 objects with continuum $S/N > 5$. We used the IDL program MPFIT (Markwardt 2009) with the initial starting values of continuum flux level, line centroid, EW and Gaussian FWHM for each component estimated from the program *splot* in IRAF. We fixed the doublet wavelengths at the rest-wavelength ratio and forced the FWHM of each doublet member to be identical as well. The bottom panel of Figure 3 shows the fitted individual C IV doublet members (blue and magenta dotted lines) and the overall fit to the absorption profile (red dotted line) in the 1:1 case.

We iterated the fitting over a narrower wavelength range: $\text{centroid} - 4\sigma < \lambda < \text{centroid} + 4\sigma$, where the centroid and σ were, respectively, the returned central wavelength and standard deviation of the best-fit Gaussian

⁴ Although the determination of best-fit stellar models is not robust for objects with continuum $S/N < 5$, the composite resulting from including these low S/N spectra shows no systematic bias in interstellar C IV absorption.

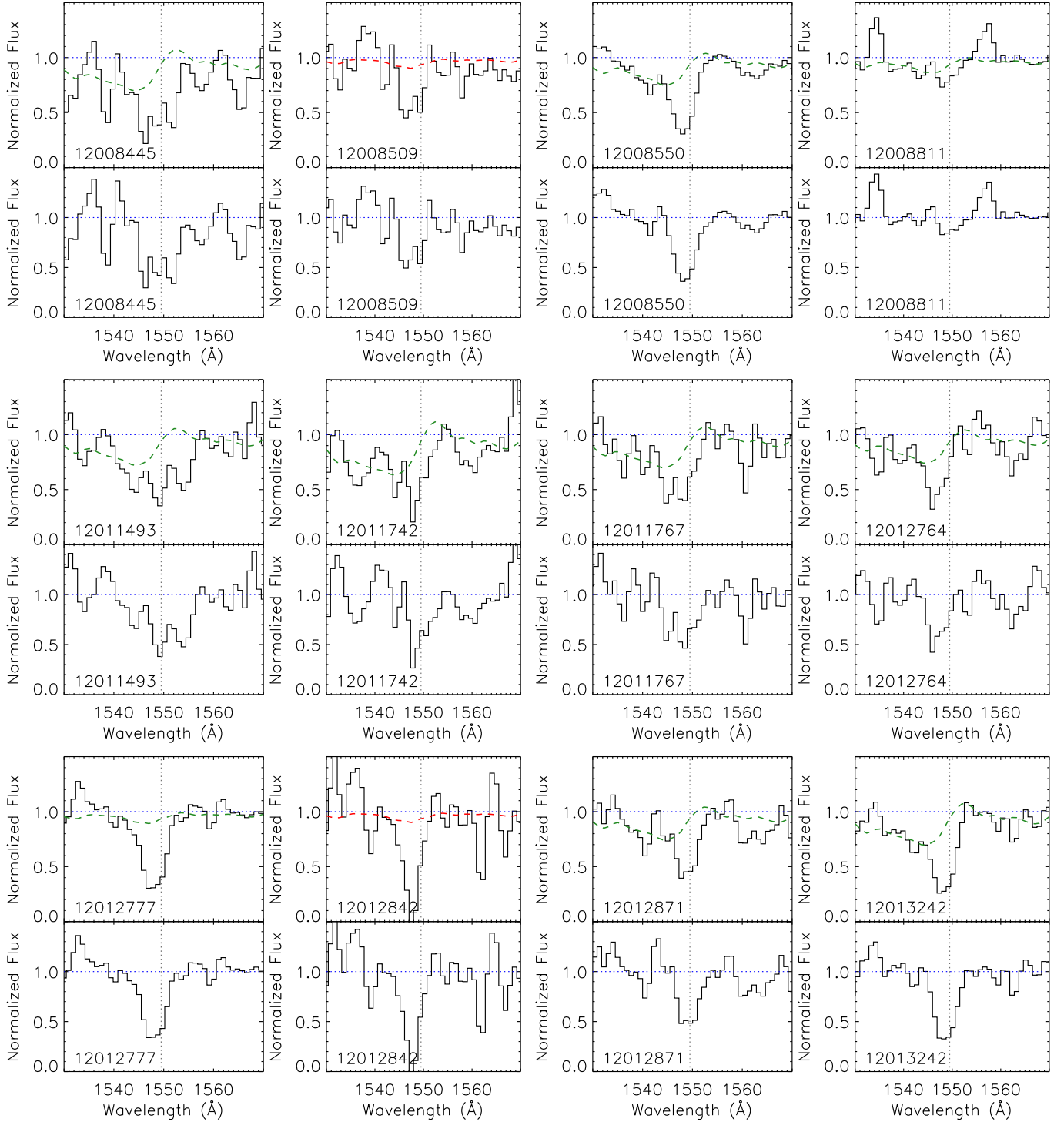


FIG. 4.— Continuum-normalized spectra (top) and spectra normalized by the best-fit stellar model (bottom) for 32 objects with continuum $S/N > 5$ and C iv EW measurements $> 3\sigma$, showing individual detection of C iv absorption. The blue horizontal dotted line indicates the continuum level, the gray vertical dotted line suggests the rest-frame wavelength of blended C iv doublet in the 1:1 case (1549.5 Å). The dashed line shows the best-fit stellar model for each object. A green dashed line indicates that the object was bracketed with neighboring metallicities, which were linearly combined to determine the best-fit stellar model. A red dashed line indicates that the object failed to be bracketed with neighboring metallicities, so the best-fit stellar model from Leitherer et al. (2010) was either $0.05Z_{\odot}$ or $2.0Z_{\odot}$.

profile from the initial MPFIT fit to the C iv doublet over 1540Å to 1560Å. We then determined the significance of the C iv EW in each object and identified 34 out of 46 objects with C iv detection $> 3\sigma$ in the sample for the study of individual velocity shifts.

There were 2 objects, 32019861 and 32020769, showing excessive absorption on the red side of C iv (red asymmetry). In either the 1:1 or 2:1 case, profiles with C iv $\lambda 1550$ stronger than C iv $\lambda 1548$ are unphysical. Possible sources of systematic error leading to this situation are associated

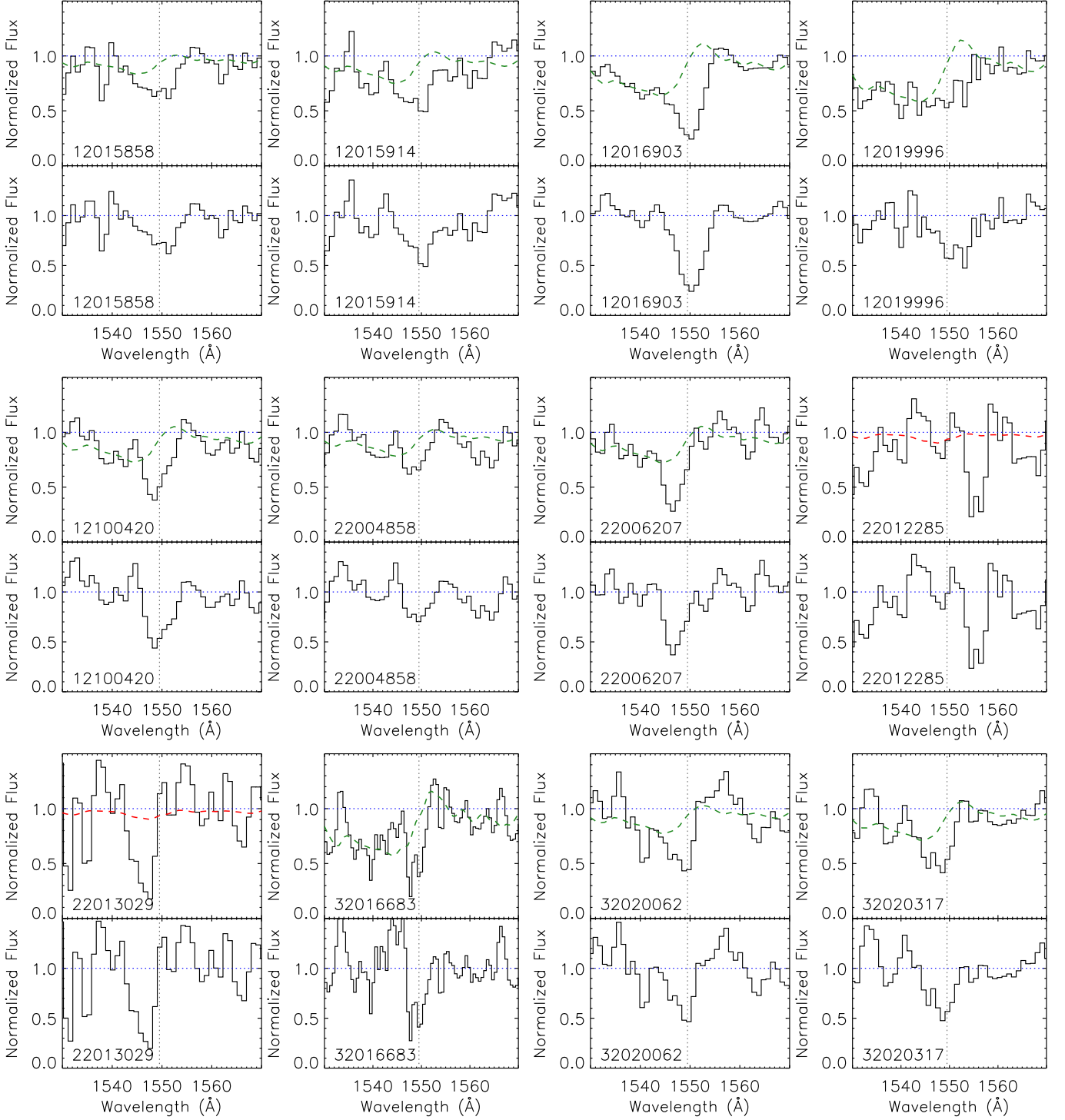


FIG. 4 (CONT.).— Continuum-normalized spectra (top) and spectra normalized by the best-fit stellar model (bottom) for 32 objects with continuum $S/N > 5$ and C IV EW measurements $> 3\sigma$, showing individual detection of C IV absorption. The blue horizontal dotted line indicates the continuum level, the gray vertical dotted line suggests the rest-frame wavelength of blended C IV doublet in the 1:1 case (1549.5 Å). The dashed line shows the best-fit stellar model for each object. A green dashed line indicates that the object was bracketed with neighboring metallicities, which were linearly combined to determine the best-fit stellar model. A red dashed line indicates that the object failed to be bracketed with neighboring metallicities, so the best-fit stellar model from Leitherer et al. (2010) was either $0.05Z_{\odot}$ or $2.0Z_{\odot}$.

with continuum fitting, best-fit stellar model determination and sky noise. We flagged and excluded these two objects from further study (gray squares in the top-right and the bottom-left panels in Figure 1). The final sample

of robust C IV detections includes 32 objects, of which the continuum-normalized spectra, and the spectra normal-

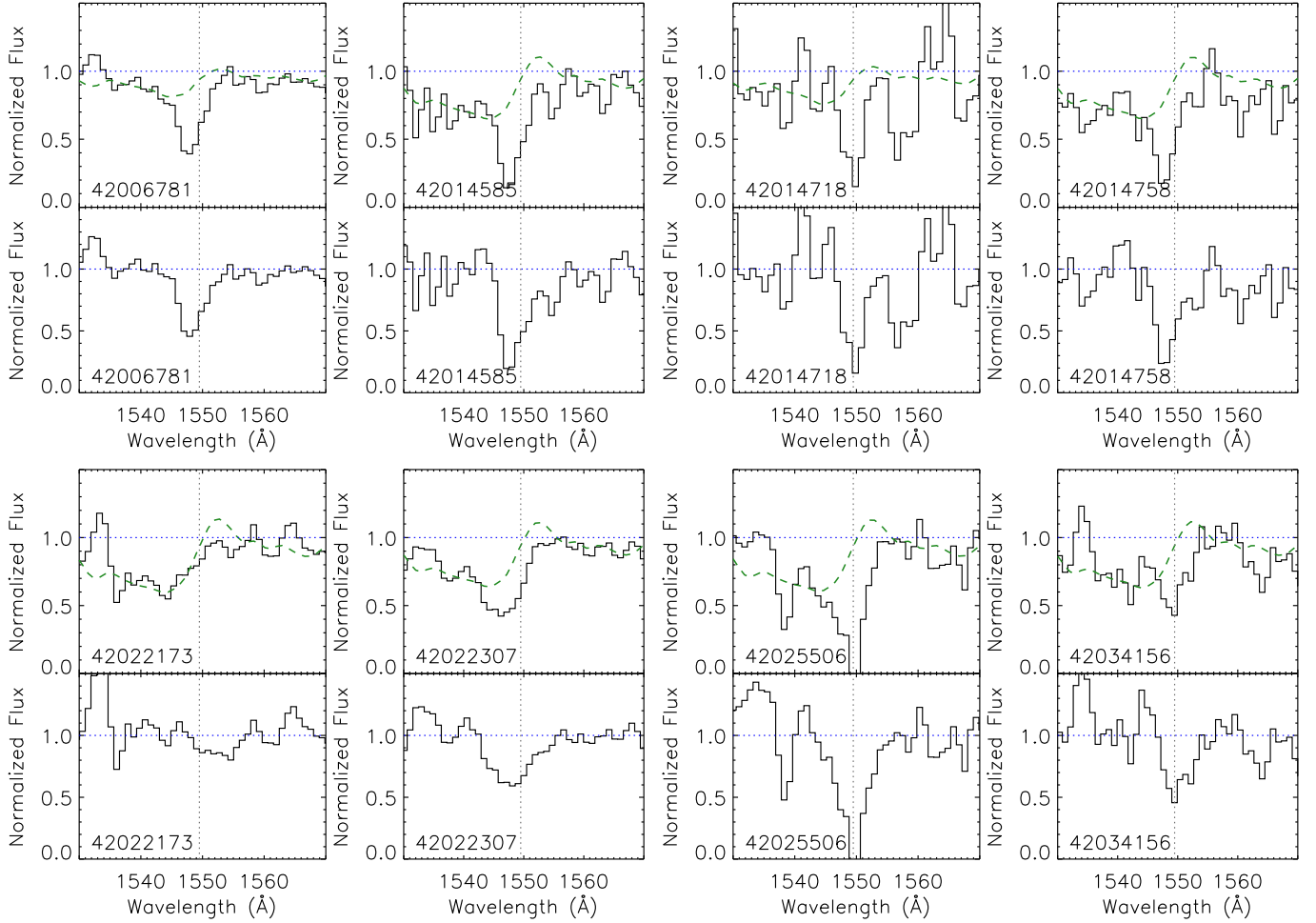


FIG. 4 (CONT.).— Continuum-normalized spectra (top) and spectra normalized by the best-fit stellar model (bottom) for 32 objects with continuum $S/N > 5$ and C IV EW measurements $> 3\sigma$, showing individual detection of C IV absorption. The blue horizontal dotted line indicates the continuum level, the gray vertical dotted line suggests the rest-frame wavelength of blended C IV doublet in the 1:1 case (1549.5 Å). The dashed line shows the best-fit stellar model for each object. A green dashed line indicates that the object was bracketed with neighboring metallicities, which were linearly combined to determine the best-fit stellar model. A red dashed line indicates that the object failed to be bracketed with neighboring metallicities, so the best-fit stellar model from Leitherer et al. (2010) was either $0.05Z_{\odot}$ or $2.0Z_{\odot}$.

ized by the best-fit stellar model are shown in Figure 4.⁵ The same sets of spectra are shown in Figure 5 for the 14 objects with continuum $S/N > 5$ and C IV EW $< 3\sigma$.

3.2. Measurement of Low-Ionization Lines

Multiple far-UV low-ionization lines fall in the vicinity of C IV, and are covered in our LRIS spectra. These include Si II $\lambda 1526$, Fe II $\lambda 1608$ and Al II $\lambda 1670$. We measure these features and compare the kinematics of different phases of interstellar gas.

We defined our far-UV low-ionization line sample in an analogous manner to that of C IV. We selected objects from the sample of 93 galaxies with C IV coverage and

⁵ Dividing out the stellar absorption has the largest effect on the blue side of the C IV profile, tending to make the inferred centroid of interstellar C IV more redshifted compared to that of the overall C IV absorption profile. Normalizing by the stellar model changes the inferred C IV centroid velocities by a few tens up to ~ 150 km s^{-1} , depending on the relative strengths of stellar and interstellar C IV absorption. Division of the best-fit stellar model minimizes the contamination from stellar absorption and thus provides a more robust description of interstellar C IV absorption.

required continuum $S/N > 5$ in the vicinity of each low-ionization feature. Accordingly, there were 46 objects in the Si II $\lambda 1526$ sample and 69 in the Fe II $\lambda 1608$ and Al II $\lambda 1670$ samples. The continuum S/N was calculated from 1570 Å to 1590 Å for Si II, and from 1690 Å to 1750 Å for Fe II and Al II. Since all of these features are singlets, we simply fit one Gaussian profile to each line. These profile fits resulted in 22 objects in the Si II sample, 14 in the Fe II sample and 44 in the Al II sample where the absorption lines were significantly detected (EW $> 3\sigma$).

To apply a consistent methodology of simple Gaussian profile fitting for analyzing both near-UV and far-UV features, we also re-measured the near-UV features presented in Martin et al. (2012) for the 93 objects with C IV coverage. These features include Mg II $\lambda 2796$, 2803 and Fe II $\lambda 2344$, $\lambda 2374$, $\lambda 2587$. To trace the kinematics of low-ionization absorption, Martin et al. (2012) fit the troughs of Fe II $\lambda 2250$, 2261, 2344, 2374, 2587 with profiles of the form $I(\lambda) = I_0 e^{-\tau(\lambda)}$, where $\tau(\lambda)$ is a Gaussian parameterized by the central wavelength, λ_0 and the Doppler parameter, b . The central wavelengths of these lines were

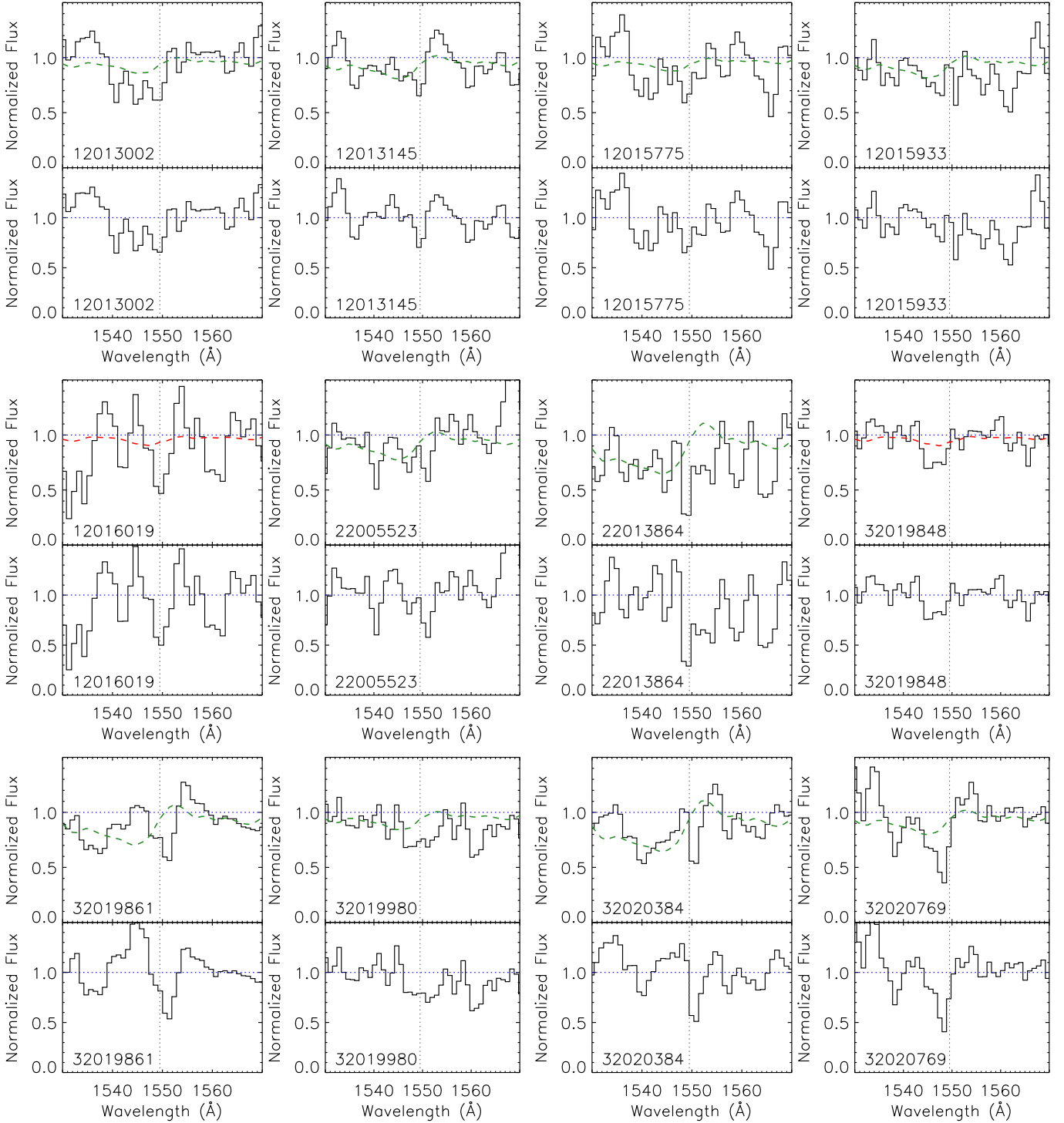


FIG. 5.— Continuum-normalized spectra (top) and spectra normalized by the best-fit stellar model (bottom) for 14 objects with continuum $S/N > 5$ and C IV EW measurements $< 3\sigma$, showing individual C IV absorption profiles. Legends are the same as in Figure 4.

tied together to define a single-component Doppler shift V_1 , and the optical depths were also tied by the ratio of their oscillator strengths. Fe II λ 2382 and λ 2600 may suffer from significant emission filling and were excluded from the fitting (see the text about Fe II λ 1608 in Section 4.1).

In our simple Gaussian fits of the near-UV Fe II features, we further excluded the weak transitions

Fe II λ 2250, λ 2261 (with oscillator strengths 14.2 and 13.3 times lower than that of Fe II λ 2374, respectively) as they provided little constraint on the velocity shift. We fixed the wavelength centroid ratios at their rest-frame values and assumed identical profile widths for all fitted near-UV Fe II lines.⁶ On the other hand, we set the

⁶ Tying the centroids introduced no systematic offset to the ve-

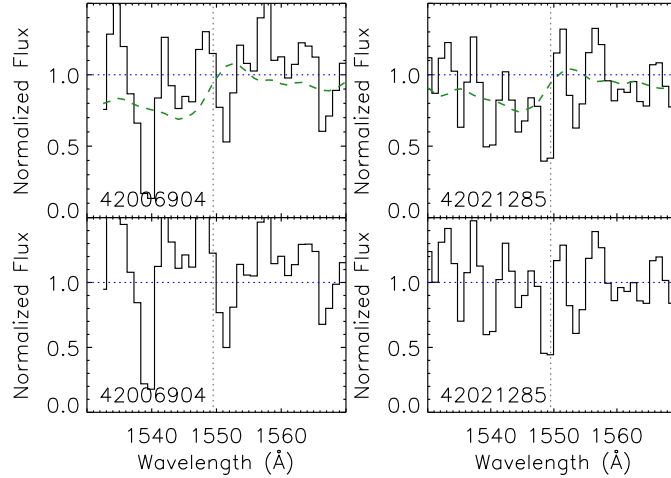


FIG. 5 (CONT.).— Continuum-normalized spectra (top) and spectra normalized by the best-fit stellar model (bottom) for 14 objects with continuum $S/N > 5$ and C IV EW measurements $< 3\sigma$, showing individual C IV absorption profiles. Legends are the same as in Figure 4.

centroids and widths of Mg II to float freely and fit the doublet wherever the χ^2 reaches a minimum, to accommodate the effects of Mg II emission filling. Specifically, the red parts of the Mg II $\lambda 2796$ and Mg II $\lambda 2803$ absorption profiles may be washed out by different amounts due to Mg II resonant emission. Therefore, the centroids of the doublet members do not necessarily show a fixed wavelength ratio and the widths may also not be the same (Martin et al. 2012). Table 1 lists the velocity shift of the measured lines (C IV, Al II $\lambda 1670$, Si II $\lambda 1526$ and near-UV Fe II) of individual objects derived from Gaussian fitting, as well as the near-UV Fe II velocity shifts from Martin et al. (2012).

4. KINEMATICS

To investigate whether the high-ionization kinematics differ from those of low-ionization lines, we compare the velocity shifts of C IV and near-UV Fe II and Mg II lines in Section 4.1. We also compare the low-ionization kinematics traced by both far-UV and near-UV lines, and discuss possible interpretations for the observed discrepancies in Section 4.2.

4.1. C IV vs. Near-UV lines

In order to compare the kinematics of C IV with those of the low-ionization lines, we calculated the velocity shifts for C IV in the 1:1 case and the near-UV Fe II lines. We define these velocity shifts, respectively, as $V_{1:1}$ and $V_{\text{nuvFe II}}$. In Figure 6, the black circles (28 objects) represent objects with robust measurements for both C IV and near-UV Fe II features (continuum $S/N > 5$ and EW $\geq 3\sigma$). Two objects stand out as having significantly redshifted C IV centroid velocities. One object, 22012285, is extremely redshifted with a velocity of $+1162 \text{ km s}^{-1}$. We interpret the C IV redshift of this object with caution, as the absorption (while formally significant), may be caused by systematic oversubtraction of the sky spectrum. Another object, 42022173 has a C IV velocity of

locity measurements of the near-UV Fe II features. Velocity shifts inferred from tied centroids were consistent with those based on fits to individual near-UV Fe II profiles. The resulting Fe II velocity shifts were consistent with those in Martin et al. (2012)

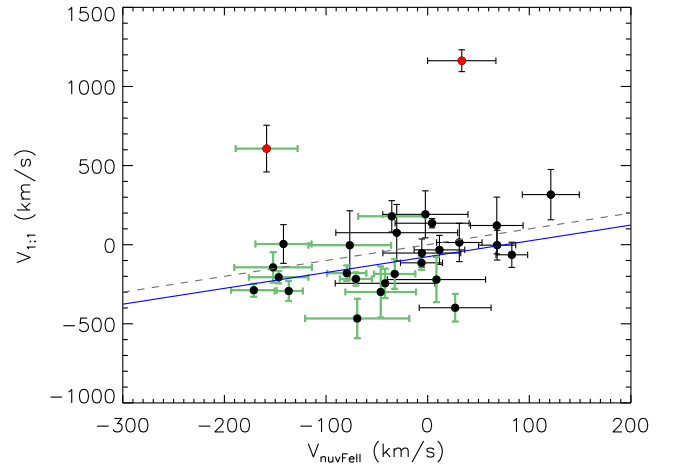


FIG. 6.— Comparison between C IV and near-UV Fe II centroid velocity shifts. There are 28 objects with continuum $S/N > 5$ and EW detections of both C IV and near-UV Fe II $> 3\sigma$. The 1:1 doublet ratio is assumed in modeling the C IV feature. The median velocity shift for C IV and near-UV Fe II (excluding 2 outliers, 22012285 and 42022173, marked in red circles) is -64 km s^{-1} and -30 km s^{-1} , respectively. The green error bars indicate 1-sigma outflows for corresponding transitions. The gray dashed line marks where $V_{1:1}$ and $V_{\text{nuvFe II}}$ are equal, and the blue solid line presents the best linear fit with the slope fixed at 1. The offset between the gray and blue lines is $-76 \pm 26 \text{ km s}^{-1}$ ($V_{1:1} - V_{\text{nuvFe II}}$). The uncertainty on the best-fit intercept were estimated from Monte Carlo methods.

$+607 \text{ km s}^{-1}$ which could be due to systematics in the normalization of the stellar wind component. The best-fit stellar model for this object (bracketed by models with $0.4Z_{\odot}$ and $1.0Z_{\odot}$), while based on the blueshifted stellar absorption profile, overproduces C IV emission at $\sim 1552 \text{ \AA}$. Therefore, after division by the best-fit model, some apparent interstellar absorption remains on the red side of the C IV profile. It is not clear whether this absorption is real or an artifact of the mismatch between model and data. Given the potentially large uncertainties associated with these two objects, we removed them from the sample when deriving the statistical properties.

After eliminating these 2 outliers, we find that 50%

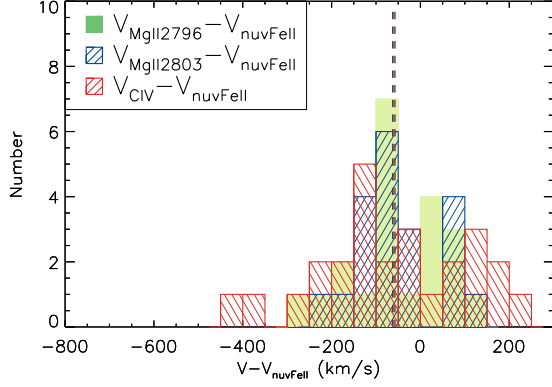


FIG. 7.— Histogram of C IV, Mg II, and Fe II velocity differences. Velocity differences are only plotted for objects with continuum $S/N > 5$ and $EW > 3\sigma$ detection for C IV and near-UV Fe II lines (red histogram, 26 objects, excluding 22012285 and 42022173), and Mg II and near-UV Fe II lines (green and blue histograms, 21 and 20 objects, respectively). The vertical colored dashed lines show the median velocity difference of corresponding pairs, which are -65 km s^{-1} , -57 km s^{-1} and -63 km s^{-1} for C IV, Mg II 2796 and Mg II 2803 with respect to near-UV Fe II, respectively.

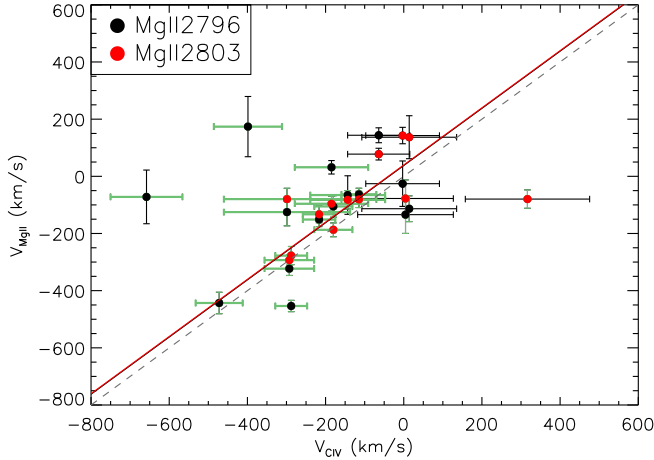


FIG. 8.— Comparison of C IV and Mg II velocity shifts. Red circles represent Mg II 2796 (15 objects) and black circles represent Mg II 2803 (13 objects). All objects shown here have continuum $S/N > 5$ and line $EWs > 3\sigma$ for both C IV and the corresponding Mg II doublet member. The green error bars indicate 1-sigma outflows for corresponding transitions. The red and black solid lines are the best-fit linear models for Mg II 2796 and Mg II 2803, respectively. The intercept for the doublet members are $+38 \pm 43 \text{ km s}^{-1}$ and $+40 \pm 18 \text{ km s}^{-1}$. The gray dashed line marks the 1:1 relation.

(27%) of the sample of 26 objects indicate 1σ (3σ) outflows. Moreover, this sample shows that C IV (median velocity shift -64 km s^{-1}) is more blueshifted than the near-UV Fe II lines (median velocity shift -30 km s^{-1}), with a median velocity difference, $V_{1:1} - V_{\text{nuvFe II}}$, of -65 km s^{-1} . Furthermore, the best-fit linear model (measurement errors considered) gives an intercept of $-76 \pm 26 \text{ km s}^{-1}$ with a fixed slope at 1, which confirms the larger blueshift of C IV at the ~ 3 -sigma level. The error bar on the best-fit intercept was estimated using Monte Carlo methods. Specifically, we bootstrap resampled the velocity shifts, $V_{1:1}$ and $V_{\text{nuvFe II}}$, of these 26 objects

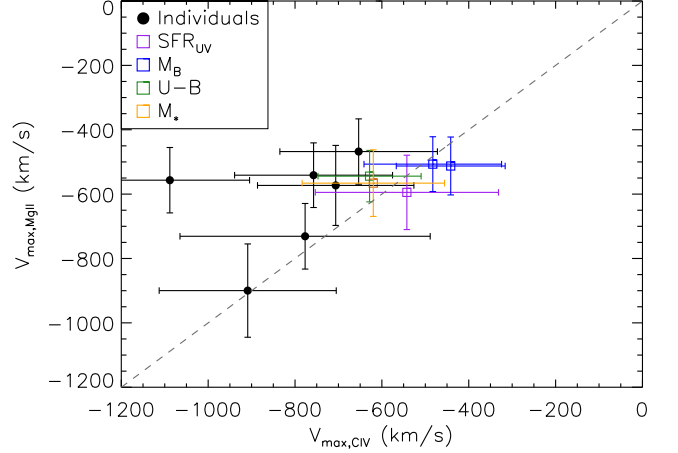


FIG. 9.— Comparison between C IV and Mg II V_{max} for resolved blue wings. The black dots represent individual objects with the highest continuum $S/N (> 10.0)$, and the colored open squares are from the composite spectra (purple, blue, green, yellow for SFR, M_B , $U-B$ and M_* , respectively) described in Section 5. The gray dashed line indicates where the two velocities are equal, and all objects fall close to the 1:1 line but the outlier 42022307.

and performed an inverse-squared weighted linear regression to the bootstrap sample. The process was repeated 100 times and the standard deviation of the intercept distribution was taken as the corresponding uncertainty. Finally, at least as large a fraction of C IV absorption profiles shows a blueshift with respect to the systemic velocity (69 % for $V_{1:1} < 0 \text{ km s}^{-1}$), compared with 65 % of the near-UV Fe II profiles (Martin et al. 2012).

Although the larger blueshift of C IV may suggest that the highly-ionized gas is in fact traveling at a slightly higher speed, a close investigation of the kinematics of Mg II absorption reveals another possibility. Figure 7 shows histograms of the velocity differences between C IV and near-UV Fe II ($V_{1:1} - V_{\text{nuvFe II}}$, red, 26 objects, excluding 22012285 and 42022173) and individual Mg II doublet members and near-UV Fe II ($V_{\text{Mg II}2796} - V_{\text{nuvFe II}}$, green, 21 objects and $V_{\text{Mg II}2803} - V_{\text{nuvFe II}}$, blue, 20 objects), where all the lines have a continuum $S/N > 5$ and $\geq 3\sigma$ absorption detection. We note that the sample here comparing C IV and near-UV Fe II is the same as that used in Figure 6. The dashed lines of corresponding colors indicate the median velocity shift between C IV and Fe II, between Mg II 2796 and Fe II and between Mg II 2803 and Fe II, respectively. The median values of these three distributions are very close to each other, suggesting that the velocity shift of C IV is nearly identical to that of Mg II.

Moreover, when directly comparing the velocity shifts derived from C IV and Mg II (Figure 8), we find that the data points scatter around the 1:1 line despite a few outliers. We note that while the best-fit intercepts give $\sim 40 \text{ km s}^{-1}$ for both Mg II doublet members ($+38 \pm 43 \text{ km s}^{-1}$ and $+40 \pm 18 \text{ km s}^{-1}$ for Mg II 2796 and Mg II 2803, respectively), this result does not necessarily suggest that C IV is more blueshifted than Mg II, given the small size of the sample. In fact, we find that the blueshift (derived from centroid velocities) of C IV is on average similar to that of Mg II when combining both Figure 7 and 8. As the Mg II profile is significantly

affected by interstellar emission filling, a natural conclusion is that C IV, another resonant line showing a similar velocity shift, may be similarly affected.

For a better understanding of the blueshift of C IV, we further studied the blue wing of the absorption trough. We focused on the extent to which measurable absorption extends blueward of the line centroid by calculating the maximum velocity, V_{max} . V_{max} is defined with respect to the blue side of the absorption profile where the measured flux meets with the spectral continuum at the 1σ level (Martin et al. 2012), and represents the largest velocity at which there is measurable absorption, regardless of the shape of the absorption trough.

To obtain V_{max} and the associated error bars, we perturbed the spectrum at each wavelength with a Gaussian random variable determined by the corresponding error spectrum, measured V_{max} in the perturbed spectrum, and then repeated the process 500 times for each object. We then calculated the average V_{max} and assigned the error bars as the larger of the standard deviation of the V_{max} distribution or half the pixel width (Martin et al. 2012). We determined V_{max} for C IV and Mg II in both the composite spectra (in different bins of galaxy properties, see Section 5) as well as 10 individual objects with the highest continuum S/N , as plotted in Figure 9. Note that we only included V_{max} for the resolved line wings which required V_{max} to be more significantly blueshifted than -282 km s^{-1} for the 600-line spectra, or -435 km s^{-1} for the 400-line spectra.⁷ Nearly all the points lie on the 1:1 line, indicating that the V_{max} for C IV and for Mg II are statistically the same. The only outlier is 42022307, which has a $V_{max, \text{C IV}} < -1000 \text{ km s}^{-1}$. We flagged this object since the C IV absorption is unusually broad, and the Mg II measurement is also not robust due to a sky line residing just bluewards of Mg II $\lambda 2796$.

In summary, the small but significant blueshift of C IV relative to near-UV Fe II suggests either the highly-ionized gas is faster-moving, or else the kinematics of low and high ions are in general consistent while the red side of the interstellar absorption trough is filled up from the C IV resonant emission. Although we favor the latter case as C IV shows a similar blueshift to that of Mg II, further studies at both higher resolution and S/N are needed to break the degeneracy.

4.2. Far-UV vs. Near-UV lines

In order to establish a velocity frame traced by far-UV absorption lines, we also plotted Si II $\lambda 1526$, Fe II $\lambda 1608$ and Al II $\lambda 1670$ against the near-UV Fe II lines. From Figure 10, we find that Al II $\lambda 1670$ scatters around the 1:1 line (median velocity shift -5 km s^{-1}) while Si II $\lambda 1526$ displays a systematic redshift relative to the near-UV Fe II (median velocity shift $+35 \text{ km s}^{-1}$). This offset is caused by the larger error bars associated with the objects at the top left corner of the top panel of Figure 10. In fact, the intercepts for the best-fit models with slope fixed at 1.0 for Si II $\lambda 1526$ and Al II $\lambda 1670$ are, respectively,

⁷ While V_{max} is less susceptible to emission filling, many objects with continuum $S/N > 5$ and robust line measurements do not have resolved V_{max} due to the low resolution of the spectra and the intrinsic widths of the absorption lines. Therefore, using V_{max} as the main velocity indicator in our sample would significantly reduce the sample size and prevent us from drawing any statistical conclusions.

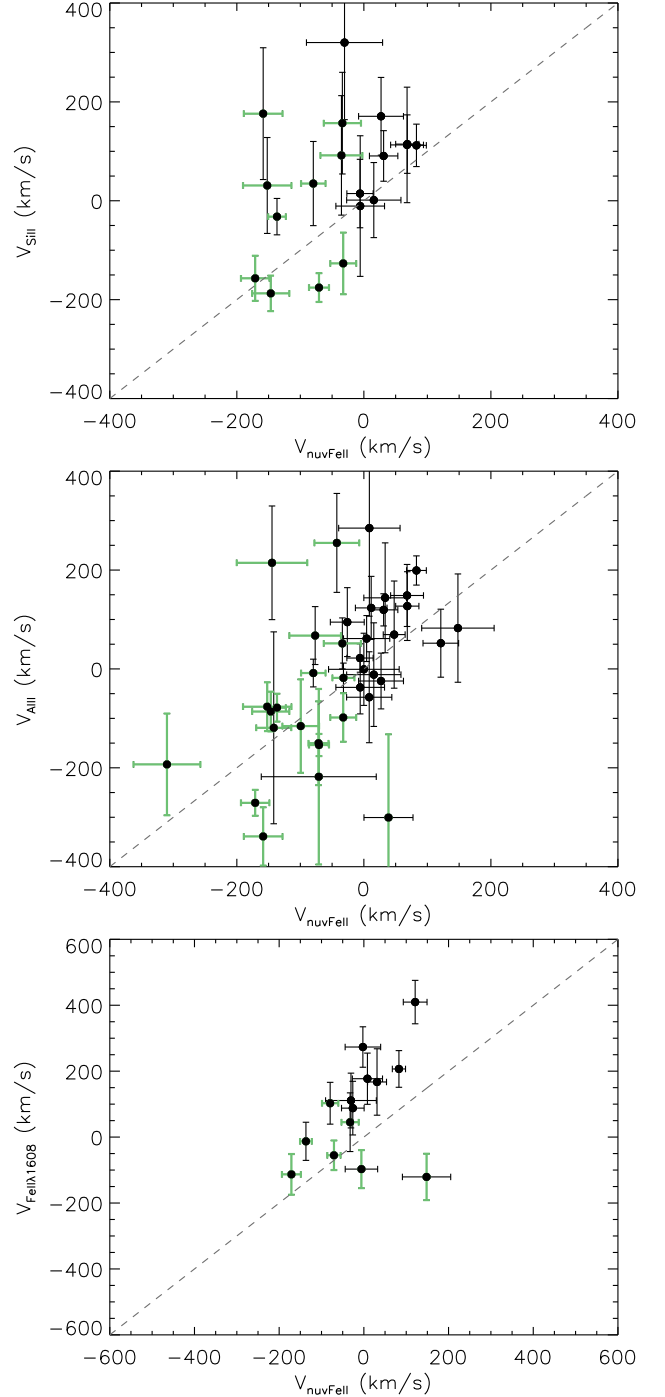


FIG. 10.— Si II $\lambda 1526$ (top), Al II $\lambda 1670$ (middle), and Fe II $\lambda 1608$ (bottom) velocity shifts compared with those from near-UV Fe II lines. Legends are the same as in Figure 6. The median velocity for Si II $\lambda 1526$, Al II $\lambda 1670$ and Fe II $\lambda 1608$ is $+35 \text{ km s}^{-1}$, -5 km s^{-1} and $+95 \text{ km s}^{-1}$, respectively. The intercept for the best linear fits with slope fixed at 1 for those lines are $+20 \pm 28 \text{ km s}^{-1}$, $+27 \pm 22 \text{ km s}^{-1}$ and $+95 \pm 33 \text{ km s}^{-1}$, respectively.

$+20 \text{ km s}^{-1} \pm 28 \text{ km s}^{-1}$ and $+27 \pm 22 \text{ km s}^{-1}$, which suggests that both Si II and Al II have velocities that are roughly consistent on average with those of the near-UV Fe II lines. Therefore, we claim that the velocity shifts traced by far-UV Si II and Al II in general agree with that traced by near-UV Fe II lines despite larger uncertainties

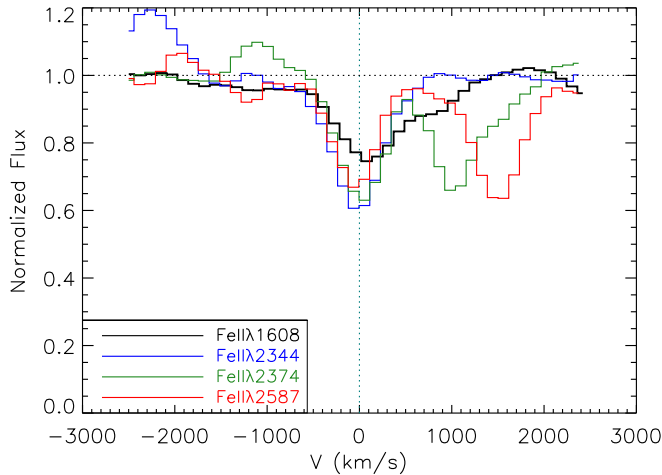


FIG. 11.— The stacked velocity profile of Fe II λ 1608 and Fe II λ 2344, 2374, 2587 for objects observed in the 400-line masks with continuum $S/N > 5$ (65 objects). The black line shows the absorption profile of Fe II λ 1608, and those of Fe II λ 2344, Fe II λ 2374 and Fe II λ 2587 are shown in blue, green and red, respectively. The dotted horizontal line marks the expected continuum level, and the dotted vertical line indicates the systemic velocity.

associated with the velocity measurements of Si II λ 1526.

It is worth noting that Fe II λ 1608, on an individual basis, appears to be significantly more redshifted relative to C IV (median $V_{\text{Fe II } \lambda 1608} - V_{\text{C IV}} = +161 \text{ km s}^{-1}$), and near-UV Fe II lines (median $V_{\text{Fe II } \lambda 1608} - V_{\text{Fe II } \lambda 2344} = +124 \text{ km s}^{-1}$ median). To investigate the reason for the relative redshift of Fe II λ 1608, we constructed a composite spectrum and compared the absorption profiles of both Fe II λ 1608 and the near-UV Fe II lines. We selected a subset of 65 galaxies, which were observed with 400-line masks (to ensure the same resolution), with continuum $S/N > 5$ in the vicinity of the near-UV Fe II features from 2400 Å to 2550 Å. We then stacked individual continuum-normalized spectra, and extracted the median value at each wavelength to create a composite spectrum. In Figure 11, Fe II λ 1608, 2344, 2374 and 2587 are plotted with respect to their rest wavelengths using black, blue, green and red lines, respectively. While there is an agreement among the velocity profiles of Fe II λ 2344, 2374, 2587, Fe II λ 1608 shows an extended wing on the red side at $\sim +800 \text{ km s}^{-1}$, making the fitted centroid redshifted compared to the other Fe II lines.

One plausible interpretation of this profile is that Fe II λ 1608 suffers less emission filling than the other near-UV Fe II lines. The continuum photons emitted by galaxies can be absorbed by the interstellar medium (ISM) and re-emitted in random directions. The electrons, after getting excited to a higher energy level from the ground state, can either decay back to the ground state (resonant emission) or to an excited ground state (fluorescent emission). The resonant emission cannot cancel out the resonant absorption exactly because of different Doppler velocities of the emitting and absorbing gas, thus we have to consider the extent to which the resonant emission, usually expected in galaxy spectra, fills the absorption trough and results in a more blueshifted absorption profile than it would otherwise (Prochaska et al. 2011; Martin et al. 2012). Based on the Einstein A coefficients of the resonant and fluorescent emission, following the

absorption in the Fe II λ 1608 resonant transition, only 26% of the photons are redirected into fluorescent emission lines at Fe II* λ 1618.47 (22%) and Fe II* λ 1625.91 (4%). In comparison, Fe II λ 2382 absorption results in no fluorescent emissions (i.e., all photons return to the ground state exclusively through resonant emission), and the fractions of fluorescent emission of the Fe II λ 2344, 2374, 2587 and 2600 resonant transitions are 35%, 86%, 67%, 13%, respectively.⁸ Thus emission filling is apparently more significant for the Fe II λ 1608 profile than for the near-UV Fe II lines used in Martin et al. (2012), and is only slightly less of an issue than for the lines excluded (i.e., Fe II λ 2382 and Fe II λ 2600). Since emission filling should affect Fe II λ 1608 more than the other lines plotted, and, if anything, should result in a larger blueshift due to more emission filling on the red side of the absorption profile (in contract to what is observed), this process clearly does not provide an explanation for the discrepant kinematics between Fe II λ 1608 and the near-UV Fe II features.

Another possible explanation is additional absorption by a nearby resonant transition, i.e., Fe II λ 1611, at the red edge of Fe II λ 1608. Fe II λ 1611 has an oscillator strength $\sim 2.5\%$ that of Fe II λ 1608 and gives additional absorption at $\sim +500 \text{ km s}^{-1}$ when blended with the Fe II λ 1608 line. Meanwhile, inspection of the Leitherer et al. (2010) far-UV spectra indicates that stellar photospheric Fe IV absorption at $\sim 1610 \text{ Å}$ may also contribute to the redshifted profile of Fe II λ 1608 (Dean & Bruhweiler 1985; Leitherer et al. 2010, private communication). Due to the potential contamination from Fe II λ 1611 (more than 2.5% if the Fe II lines are not optically thin), Fe IV and possibly additional unidentified absorption lines, we do not use Fe II λ 1608 for determining low-ionization absorption kinematics.

5. GALAXY PROPERTIES

While the study of individual velocity shifts can only be performed on objects with high S/N and significant line detections, composite spectra enable us to utilize the full sample and study the overall correlations between spectral and galaxy properties. Moreover, using composite spectra potentially enables the measurement of weak absorption lines by increasing continuum S/N (continuum S/N increased by a factor of \sqrt{N} , where N is the number of objects that go into each composite spectrum).

Within the coverage of the DEEP2/LRIS spectra, there reside multiple weak far-UV transition lines, including Ni II λ 1741, 1751, Si II λ 1808 and Al III λ 1854, 1862, which we were not able to measure robustly in individual spectra. Composite spectra enabled the measurement of these weak lines in addition to the strong UV absorption lines we described before (Si II λ 1526, C IV λ 1548, 1550, Al II λ 1670, Fe II λ 2344, λ 2374, λ 2587

⁸ While theoretical wind models (e.g., Prochaska et al. 2011) predict a difference in kinematics among the near-UV Fe II lines (i.e., Fe II λ 2382 and Fe II λ 2600 being more blueshifted than Fe II λ 2374 and Fe II λ 2587), we do not observe this trend in our sample. Instead, Fe II λ 2382 and Fe II λ 2600 display similar centroid velocities on average to those of Fe II λ 2344, Fe II λ 2374 and Fe II λ 2587, suggesting that Fe II features are less subject to emission filling than Mg II (see also Erb et al. 2012, for a full discussion of emission filling in Fe II and Mg II features).

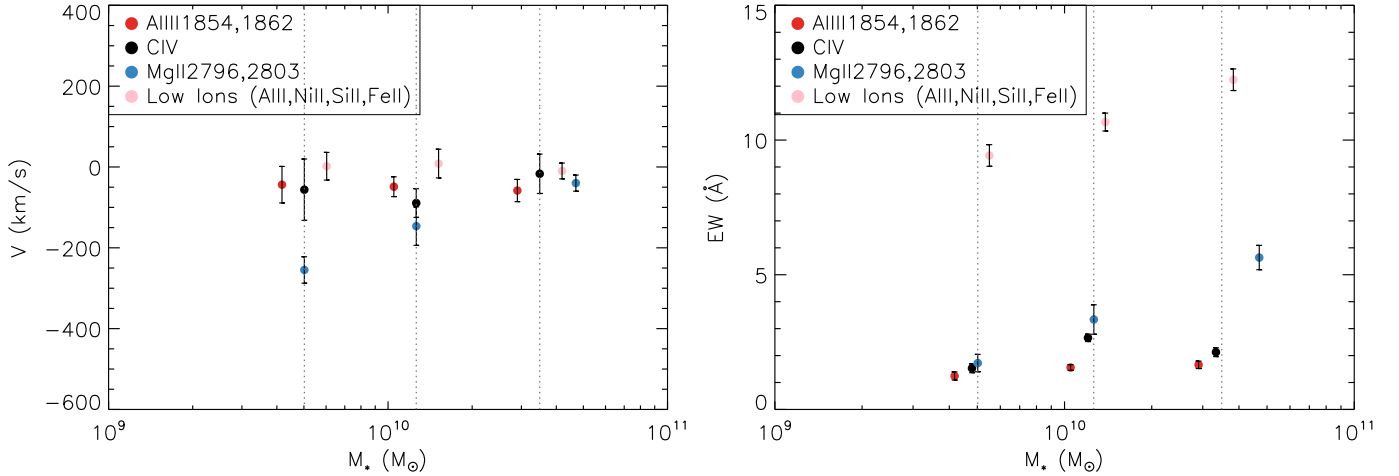


FIG. 12.— Interstellar absorption velocity shift and EW vs. stellar mass in the composite spectra. The median stellar mass of each bin is indicated with the vertical gray dashed lines, and the data points are offset horizontally for display purposes. The black points represent C IV measurements, while the red points indicate the Al III doublet. The light pink points indicate a set of low-ionization lines (Si II λ 1526, Al II λ 1670, Si II λ 1741,1751, Si II λ 1808 and near-UV Fe II), representing the average velocity shift of the total EW. Finally, the Mg II doublet, as isolated from the other low-ionization lines, is shown by blue points.

and Mg II λ 2796, 2803). In light of the fact that outflows have a multi-phase structure, we included Al III measurements here to explore the kinematics of an intermediate-ionization phase in the composite spectra.

To investigate the correlation between the kinematics and strength of both high- and low-ionization lines and galaxy properties, we divided all 93 objects with C IV coverage into three bins in stellar mass, $U-B$ color and B -band luminosity, and two bins in SFR, SFR surface density and sSFR, given that only 25 objects in the AEGIS field have SFR_{UV} measurements. Each bin contained nearly the same number of galaxies. To create the composite spectra, we used individual continuum-normalized spectra for measurements of the low-ionization lines and spectra normalized by the Leitherer et al. (2010) stellar models for measurements of C IV and Al III. Al III, like C IV, has a complex profile including both the absorption from stellar winds and the ISM. However, since the stellar wind component contributing to the Al III profile is several times weaker than that of C IV (Leitherer et al. 2010), we simply used the blue wing of the C IV feature to determine the stellar absorption affecting both C IV and Al III. For each object, we divided the continuum-normalized spectrum by the best-fit stellar model determined from C IV (described in Section 3.1). We then smoothed all 600-line spectra to the resolution of the 400-line spectra (for both continuum-normalized data and those normalized by the best-fit stellar models), and used the IRAF routine *scombine* to extract the median value of the normalized composite spectrum for each bin. To create the corresponding error spectrum for each composite spectrum, we bootstrap resampled each bin and perturbed each spectrum in the bootstrap sample according to its own error spectrum. The perturbed spectra in the bootstrap sample were then combined to create a new composite spectrum. The process was repeated 100 times and the standard deviation of these 100 fake composites at each wavelength was taken to create a composite error spec-

trum for each bin. With this approach, we accounted for both sample variance and measurement uncertainty.

Both centroid velocity and V_{max} can be used to probe the kinematics of interstellar gas. Although V_{max} is not subject to potential emission filling, it is not resolved in all the bins of the stacked spectra, especially for C IV. On the other hand, the centroid velocity is well measured for features in all stacked spectra. Accordingly, we used centroid velocity inferred from the absorption features for the kinematic analysis in this section.

We fit the C IV, Si II λ 1526, λ 1808, Al II, Ni II, Al III, near-UV Fe II and Mg II features in the stacked spectra with Gaussian profiles using MPFIT to measure their centroids and EWs. We required all centroids of the doublet members and the near-UV Fe II lines to be fixed with the exception of Mg II, for the reason stated in Section 3.2. We also forced the FWHM of each C IV and near-UV Fe II member to be the same. We allowed the width of doublet members to float freely for Ni II and Al III, since the profile of these weak features is significantly affected by noise, and thus may deviate from 1:1 width ratio.⁹

Since we found no significant correlations between the spectral properties (blueshift and strength) of any lines listed above and $U-B$ color or B -band luminosity in the composite spectra, we only discuss stellar mass, SFR and sSFR in this section where systematic trends have been observed.

5.1. Stellar Mass

The plot of measured velocity shift and EW versus stellar mass is shown in Figure 12. The median stellar mass of each bin is plotted as a gray dashed line, and the data points are offset horizontally for display purposes. We show the summed EW and average velocity shift for all low-ionization lines (Si II λ 1526, Al II λ 1670, Ni II λ 1741,1751, Si II λ 1808 and near-UV Fe II) with the exception of Mg II. Mg II is plotted separately, as the

⁹ The results do not change significantly if the FWHMs of the doublet members are fixed at 1:1 for the weak transitions.

trends it follows may be more significant due to emission filling.

In Figure 12, all lines except Mg II reside near the systemic velocity, and none but Mg II exhibits a trend between the velocity shift and stellar mass. It indicates that the blueshift of C IV, Al III and the low-ionization lines, Mg II excluded, is not sensitive to stellar mass. Mg II displays a smaller blueshift and a larger EW in galaxies with higher stellar masses. Given that $V_{max, Mg II}$ for all three stellar mass bins are similar (-519 km s^{-1} , -566 km s^{-1} and -538 km s^{-1} for the high-, medium- and low- M_* bins, respectively), this trend suggests that outflow velocity does not depend strongly on stellar mass (See also Martin et al. 2012). Rather, it results from the fact that resonant Mg II emission fills more of the absorption trough in less massive galaxies, making the observed profile more blueshifted while having a smaller EW. The strength of the low-ionization lines shows a positive correlation with stellar mass. Since massive galaxies tend to have more interstellar gas, larger covering fractions for the cold gas content in ISM lead to a deeper absorption trough for the low-ionization lines (Erb et al. 2006). C IV and Al III, on the other hand, show no significant correlations in EW, suggesting that the strength of intermediate- and high-ionization absorption lines is independent of stellar mass.

5.2. SFR

Figure 13 shows how the measured velocity shift and EW vary with SFR for absorption transitions tracing different ionization states. In the right panel, the green circles represent the total EW of only Si II $\lambda 1526$ and Al II $\lambda 1670$ for the comparison with the measurements from Lyman break galaxies (LBGs) from Shapley et al. (2003) (see Section 6.1).

We find that both the blueshift and EW of C IV increase with an increasing SFR. The same trends of both blueshift and EW with SFR also hold for the low-ionization lines, Mg II included. In addition, it is interesting that the centroids of C IV and the low-ionization lines (excluding Mg II) are *redshifted* in the low-SFR bin, and the low-ionization lines are barely blueshifted in the high-SFR bin. Figure 13 shows that the C IV properties are exclusively related to SFR, suggesting that massive star formation and associated processes drive the properties of the highly-ionized gas traced by C IV, while for low-ionization lines, the properties correlate with both SFR and stellar mass. Many studies have revealed a relationship between SFR and stellar mass in star-forming galaxies (often referred as the ‘main sequence’; Elbaz et al. 2007; Noeske et al. 2007; Kashino et al. 2013). Hence, the observed correlation between low-ionization absorption line properties and SFR may simply be a byproduct of the relationship with stellar mass. The intermediate-ionization doublet, Al III, appears to have a nearly zero velocity shift (at systemic velocity) in both bins and displays no significant correlation with SFR.

It is worth mentioning that C IV shows a larger blueshift relative to the low ions in the high-SFR bin than in the low-SFR bin. This larger differential blueshift may result from a larger contribution of shocked, collisionally ionized gas to the C IV absorption in the high-SFR bin. Alternatively, C IV may simply be more affected by emission filling at higher SFRs.

The larger blueshift of Mg II relative to that of C IV in the low-SFR bin at first seems to be inconsistent with our results stated in Section 4.1 that these two transitions display similar velocity shifts on average. However, we find that the objects that contribute to the low-SFR composite are not representative of the parent sample (93 objects with C IV coverage) in terms of C IV kinematics, and those with detected C IV tend to have less blueshifted and even significantly redshifted absorption profiles (measured velocity shifts ranged from -52 km s^{-1} to $+191 \text{ km s}^{-1}$, with a median of $+44 \text{ km s}^{-1}$).¹⁰ We are not certain at this point whether this discrepancy is due to the selection effect of a small sample (13 objects in the low-SFR bin), or whether galaxies with low SFRs are intrinsically associated with high-ionization inflows. A larger sample is required to address this question.

5.3. Specific SFR

Figure 14 shows the relation between kinematics of low-, intermediate- and high-ionization lines and sSFR. While becoming more blueshifted and stronger at higher sSFR, both C IV and the low-ionization lines (excluding Mg II) are redshifted in the low-sSFR bin and have marginally blueshifted centroids in the high-sSFR bin. Although Mg II also shows a larger blueshift at higher sSFR due to the increased effects of emission filling, its strength actually decreases at higher sSFR. The contrasting behavior of the EWs of Mg II and the other low-ionization lines can be explained in terms of the interplay between SFR and stellar mass. All low-ionization lines, Mg II included, increase in strength with both increasing SFR and stellar mass. The observed trends with sSFR (i.e., SFR/M_*) are therefore weak, and reflect a stronger dependence of Mg II emission filling on stellar mass than on SFR. The intermediate-ionization phase Al III, is not sensitive to sSFR and shows no strong correlations.

6. SUMMARY AND DISCUSSION

In this paper, we have analyzed the far-UV LRIS spectra of a sample of 93 DEEP2 galaxies at $z \sim 1$ with coverage of C IV $\lambda\lambda 1548, 1550$. We focused on 46 objects with continuum $S/N > 5$ and investigated the kinematics of highly-ionized gas in 32 objects with significant C IV detections. We have also measured low-ionization far-UV lines as well as near-UV Mg II and Fe II. We found that the typical blueshift of C IV absorption was slightly greater than that of near-UV Fe II resonant absorption lines at the ~ 3 -sigma level (intercept of the best-fit linear regression $-76 \pm 26 \text{ km s}^{-1}$), with a similar detection fraction of blueshifted C IV absorption. We

¹⁰ In order to reduce the potential bias introduced by small sample size, we did the same analysis using the Bundy SFR. Although we believe SFR_{UV} is more reliable, they only cover 25 out of 93 objects in our sample. Bundy SFRs, on the other hand, are available for all 93 objects. Given these two SFR measurements are correlated (Figure 1), the composite spectra created using the Bundy SFR should qualitatively reproduce the results derived from SFR_{UV} -generated composites. Therefore, we produced three composite spectra (low-, median- and high-SFR bins) according to Bundy SFR and each bin contained 31 objects. Again, C IV is less blueshifted than Mg II in the low-SFR_{Bundy} bin (measured C IV velocity shifts ranged from -472 km s^{-1} to $+191 \text{ km s}^{-1}$, with a median of -32 km s^{-1}). Note that the median blueshift of C IV in this case is still not as large compared to that in the sample with robust C IV measurements (-64 km s^{-1}). Hence, a larger sample cannot fully account for the discrepancy we observe.

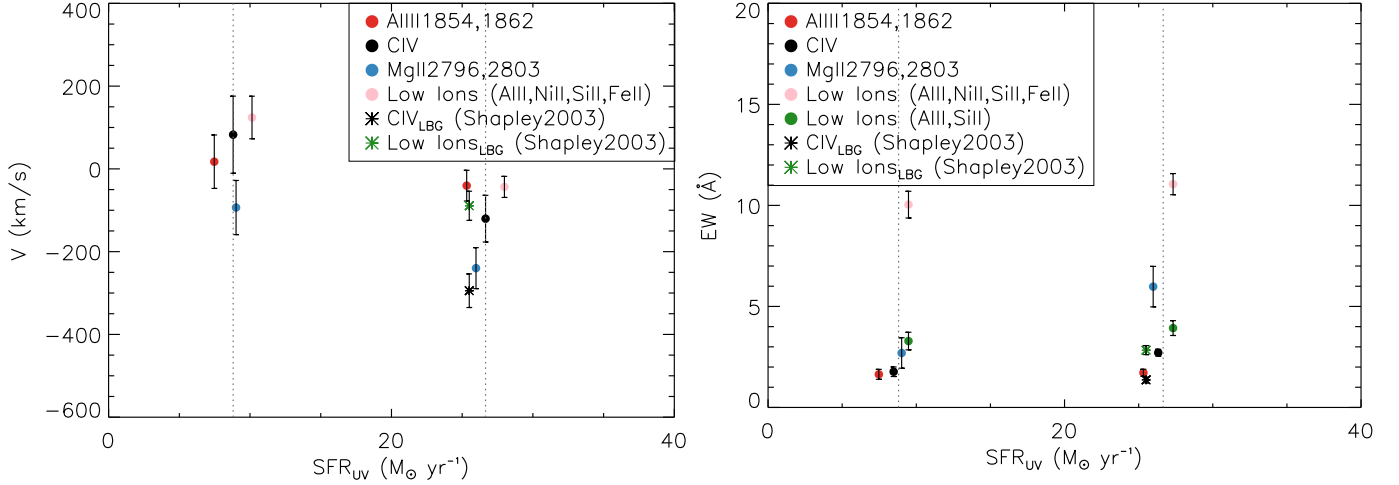


FIG. 13.— Interstellar absorption velocity shift and EW vs. SFR in the composite spectra. Legends are the same as in Figure 12. The green and black stars are measurements from the LBG composite in Shapley et al. (2003), where only Si II λ 1526 and Al II λ 1670 are available for the low-ionization line measurements. The errors for the LBG sample was estimated from fitting 500 fake composites, perturbing the returned parameters (centroids, EW) with associated error for each fake composite, and taking the standard deviation from the final distribution of the 500 perturbed centroids or EWs. The green circle in the right panel represents the total EW of Si II λ 1526 and Al II λ 1670 in the DEEP2 sample, in order to make reasonable comparison with the measurements from Shapley et al. (2003).

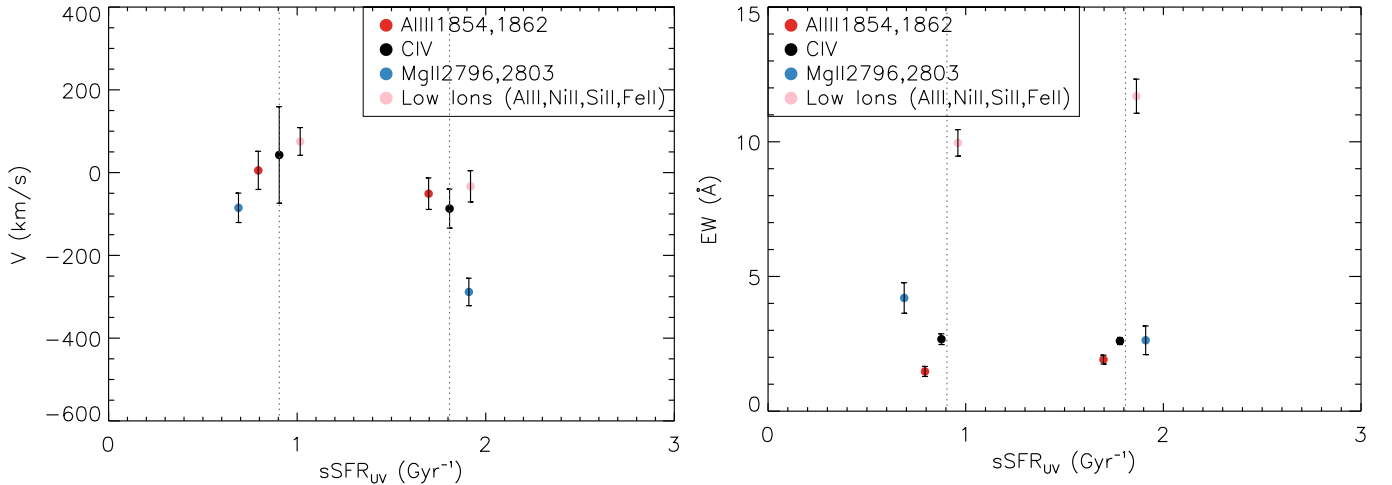


FIG. 14.— Interstellar absorption velocity shift and EW vs. sSFR in the composite spectra. The legends are the same as in Figure 12.

further compared the C IV absorption profile with that of Mg II. Given that both the centroid velocity shifts and the maximum velocities of C IV and Mg II are nearly identical, we concluded that the larger blueshift of C IV absorption with respect to the near-UV Fe II may be caused by either faster motion of the highly-ionized gas, or, more likely, filling in on the red side from resonant C IV emission in analogy to what has been observed in Mg II and Fe II (Martin et al. 2012; Kornei et al. 2012).

We also investigated the scaling relations between C IV kinematics and galaxy properties by making composite spectra of galaxies binned according to stellar mass, SFR, sSFR, SFR surface density, $U-B$ color and B -band luminosity. We found that both the blueshift and EW of C IV increase as SFR and sSFR increase, suggesting that outflowing high-ionization gas is associated with processes related to star formation, such as energy and momentum input from massive stars and their supernovae. The strength of the low-ionization lines, on the other hand,

is more correlated with the stellar mass, which can be explained by larger covering fractions and velocity dispersions of the cold phase of the ISM in more massive galaxies, due, respectively, to the greater amount of interstellar gas and overall dynamical mass. The properties of Al III are not sensitive to any of the galaxy properties we studied.

6.1. Redshift Evolution

To investigate the possible evolution of the C IV kinematics, we compared our results with the $z \sim 3$ Lyman Break Galaxy (LBG) composite from Shapley et al. (2003). The composite was constructed from 811 individual LBG spectra, and spans from 900Å to 2000Å in wavelength. Since no near-UV spectral features were available, and all the absorption lines beyond 1800Å were poorly detected in the LBG composite, we only measured C IV, Si II λ 1526 and Al II λ 1670. Due to the lack of the corresponding composite error spectrum, we estimated

the uncertainties using a method consistent with that of Shapley et al. (2003): we measured the noise from a relatively featureless range of the continuum (1700 Å to 1825 Å) and assigned this value as a constant error across the full spectrum to account for pixel variance. To account for sample variation, we fit the far-UV absorption lines in 500 fake composite spectra, which were constructed from bootstrap resampling from the original sample used for the real composite. For each fake composite, the parameters returned by MPFIT were then perturbed by the associated errors. The final error on the parameters for the real composite was derived from the standard deviation of the parameter distributions over the fake composites. SFRs for LBGs were estimated from dust-corrected rest-frame UV luminosities, combining apparent R magnitudes, and extinction based on observed $G - R$ colors. The median SFR from the LBG sample is $26 \text{ M}_\odot \text{ yr}^{-1}$ (assuming a Chabrier IMF and $H_0 = 70 \text{ km s}^{-1}$), which is close to that of the high SFR bin in the DEEP2/LRIS sample. Stellar mass and sSFR are not available for the LBGs, thus SFR is the only galaxy property we study here.

As shown in Figure 13, both C IV and far-UV low-ionization lines in LBGs have a higher blueshift yet a lower EW compared to our sample with similar SFRs. This difference may be caused by a different proportion between outflowing and interstellar gas in galaxies. Absorption from the systemic and outflowing portions of the ISM jointly contribute to the observed absorption profile. If instead, we model each absorption line (individual doublet member in the C IV case) with a two-component fit: a dominant systemic component with no Doppler shift representing the absorption from ISM, and a Doppler component characterizing the contribution from outflows (Steidel et al. 2010; Coil et al. 2011; Martin et al. 2012), the change in either component may alter the shape of the absorption trough. Lack of ISM absorption around systemic velocity results in a more blueshifted centroid as well as a smaller EW, as the LBG sample suggests.

However, this difference can also result from emission filling, especially for resonant lines like C IV. In order to investigate the real cause, we further compared the maximum velocity of C IV, $V_{\text{max,C IV}}$, in both the LBG composite and the DEEP2/LRIS sample. The measurement of $V_{\text{max,C IV}}$ in LBGs was performed in an analogous way to that described in Section 4.2. For a rough estimate of uncertainties in the LBG composite, we increased the constant error, which was derived from the continuum noise over the wavelength range of 1700 Å - 1825 Å, by a factor of two. We then measured $V_{\text{max,C IV}}$ of the LBGs in 500 fake composite spectra (the same set as described previously in this section) and derived an average value of -649 km s^{-1} . In comparison, $V_{\text{max,C IV}}$ of the high-SFR bin in the DEEP2/LRIS sample is -542 km s^{-1} with a similar SFR ($30 \text{ M}_\odot \text{ yr}^{-1}$). The larger V_{max} , along with a bluer centroid, suggests that the entire absorption profile of C IV in LBGs is shifted bluewards with less absorption, rather than only having emission filling on the red side of the absorption trough. This observed trend may arise as a consequence of a patchier systemic ISM component and a more significant Doppler component in the LBGs compared to that in the DEEP2/LRIS galaxies.

6.2. C IV vs. O VI

Our results demonstrate that low- and high-ionization interstellar absorption lines only have small differences in terms of kinematics, in the spectra of star-forming galaxies at $z \sim 1$. Objects with robust measurements of both C IV and near-UV Fe II show a median velocity difference of $V_{1:1} - V_{\text{nuvFe II}} = -65 \text{ km s}^{-1}$, and the best-fit linear regression of $V_{1:1}$ on $V_{\text{nuvFe II}}$ of this sample is characterized by an intercept of $-76 \pm 26 \text{ km s}^{-1}$, assuming a slope of unity. Moreover, given that the velocity shifts of C IV measured from both line centroids and blue wings agree with those of Mg II, we conclude that C IV, being a resonant transition like Mg II, is affected by emission filling to the same extent. Therefore, the small apparent velocity discrepancy between C IV and near-UV Fe II can be explained by filling in on the red side of the C IV absorption trough by resonant emission, instead of evidence for highly-ionized gas outflowing at a larger speed than that of gas traced by low-ionization lines.

Similar results on the relative velocity shifts between low and high ions have been reported for $z \sim 3$ LBGs and low-redshift star-forming galaxies. In the composite spectrum from Shapley et al. (2003), the high-ionization Si IV feature displays a similar mean blueshift and velocity FWHM to those of low-ionization lines, including Si II, O I, C II, Fe II, and Al II. In addition, Pettini et al. (2002) studied the kinematics of different phases in ISM using the gravitationally lensed LBG, MS 1512-cB58, with much higher spectral resolution (58 km s^{-1} FWHM). The spectrum of cB58 suggests that all the observed ion stages span the same overall range in velocity, and that the gas with the highest optical depth is blueshifted by roughly the same amount for both low (e.g., Si II, C II,) and high ions (e.g., Si IV, C IV). At low redshift, recent work by Chisholm et al. (2016) yields similar results. These authors study 37 nearby star-forming galaxies using tracers at different ionization stages (O I, Si II, Si III, and Si IV), and show that absorption lines with similar strength, regardless of ionization state, have comparable outflow velocities. These findings suggest that gas clouds traced by low- and high-ionization lines may actually be co-moving.

In apparent contrast, Heckman et al. (2001) find that high-ionization lines in general have larger outflow velocities compared to the low ions by studying the rest-far-UV spectrum of the dwarf starburst galaxy NGC 1705. One distinction highlighted by Heckman et al. (2001) is that O VI, which traces the coronal-phase gas, has broader and more blueshifted absorption profile than the low ions. Grimes et al. (2009) extended the sample to 16 local starbursts, finding similar results. Specifically, Grimes et al. (2009) detect a more significant blueshift in O VI than in the low-ionization C II, N II features, and the intermediate-ionization stage C III line, suggesting that highly-ionized gas in general has larger outflow velocities.

These seemingly contradictory conclusions are in fact due to different tracers used as ‘high-ionization lines.’ In fact, although both C IV and O VI can be produced both from cooler ($T < 10^5 \text{ K}$), photoionized gas, and hotter ($T > 10^5 \text{ K}$), collisionally ionized gas, observations and simulations suggest that the hot, collisionally ionized phase makes a more significant contribution to

circumgalactic O VI. Most observations of circumgalactic C IV (e.g., Lehner et al. 2011; Liang & Chen 2014) find that this transition arises in photoionized gas (but see Borthakur et al. 2013). In simulations of galaxies including feedback (e.g., Shen et al. 2013; Liang et al. 2015), the gas traced by O VI absorption is hotter on average, and more diffuse and spatially extended, while the gas giving rise to C IV absorption is clumpier, and traces gas at smaller galactocentric radii. In terms of line strength, although the covering fraction of both C IV and O VI decreases less rapidly in the radial direction than that of the low ions (Steidel et al. 2010; Shen et al. 2013; Liang & Chen 2014), C IV displays a sharper drop in the radial profile of column density compared to that of O VI (Liang et al. 2015). In short, both observations and simulations show that C IV and O VI probe different distributions of circumgalactic gas, and, therefore, may trace distinct outflow kinematics.

Given similar velocity shifts observed in C IV and the low ions in our sample, it is possible that the cool and warm gas, traced by the low-ionization lines and C IV, respectively, are largely co-spatial and moving at similar velocities. At the same time, these gas phases are cooler, with lower characteristic outflow velocity compared to the gas typically probed by O VI. One possible explanation is that O VI, which is a characteristic feature of starburst galaxies, is produced when hot, X-ray emitting gas interacts with cold, dense clouds in its path (Grimes et al. 2009). Meanwhile, C IV may arise from the interface layer between the low-ionization clouds and the hot, radiative cooling gas flow where O VI is seen.

6.3. Future Outlook

Investigations comparing the properties of different phases of the outflowing gas are crucial for mapping detailed multi-phase structure and estimating the overall mass loss rate through galactic winds. In this paper, we do not observe large difference in the velocity shifts between the high-ionization C IV and the low-ionization near-UV Fe II features. This result suggests that the gas traced by C IV and low ions may be co-moving, and, even co-spatial. In addition, we find that the strength of C IV scales mainly with SFR, while that of the low-ionization lines is more sensitive to stellar mass. These results indicate that the gas probed by C IV is more associated with outflows, while the low-ionization lines additionally trace the systemic ISM component in the galaxies. Considering the different cases discussed in Section 4, we propose two scenarios to explain the origin of the small blueshift interstellar C IV shows relative to near-UV Fe II lines.

If the more highly-ionized gas is indeed traveling faster, our findings suggest that although C IV and the low ions both have absorption profiles consisting of a Doppler (outflow) component and a systemic ISM component, the ISM component is dominant in the low ions while the outflow component contributes more to the C IV absorption profile. If the outflowing gas traced by C IV and by the low ions are co-moving, one would expect their outflow components to have roughly the same blueshifts. Therefore, the stronger outflow component relative to that of the low-ionization lines makes C IV show a slightly more blueshifted overall absorption profile than the low ions, as suggested by our data. Alternatively, if the larger blueshift of C IV is caused by emission filling – the sce-

nario we currently favor – our results indicate that in high-SFR galaxies more C IV absorption is produced in the ISM due to various reasons (e.g., stellar wind from massive stars, supernova explosions, shocks). In this case, the highly-ionized gas is not necessarily associated with outflows, and the apparent larger blueshift of C IV is only a result of stronger emission filling due to higher C IV column density. Future simulations studying the relation between feedback and the circumgalactic medium should be able to reproduce these results.

At the same time, it is essential to have access to spectroscopic data with higher S/N and spectral resolution in order to resolve the C IV doublet members. Such data would enable us to perform the two-component fit to individual C IV doublet members, modeling the outflow and ISM components separately. In this way, one would be able to draw more robust conclusions about the low- and high-ionization kinematics. A larger sample is also crucial to investigate the relative blueshifts shown by C IV, Mg II and near-UV Fe II. Such improvements will enable us to fully comprehend the links and distinctions among the kinematics of different gas phases in star-forming galaxies.

We thank Claus Leitherer for help with the identification of stellar absorption lines, Max Pettini for providing the stellar models and Michael Fitzgerald for suggestions about statistical methods. We acknowledge support from the David & Lucile Packard Foundation (A.E.S. and C.L.M.), and the National Science Foundation through grants AST-0808161 and AST-1109288 (C.L.M.) and CAREER award AST-1055081 (A.L.C.). We are grateful to the DEEP2 and AEGIS teams for providing both the galaxy sample and ancillary data on galaxy properties. We wish to extend special thanks to those of Hawaiian ancestry on whose sacred mountain we are privileged to be guests. Without their generous hospitality, most of the observations presented herein would not have been possible.

REFERENCES

- Bordoloi, R., Lilly, S. J., Hardmeier, E., et al. 2014, *ApJ*, 794, 130
- Borthakur, S., Heckman, T., Strickland, D., Wild, V., & Schiminovich, D. 2013, *ApJ*, 768, 18
- Bruzual, G., & Charlot, S. 2003, *MNRAS*, 344, 1000
- Bundy, K., Ellis, R. S., Conselice, C. J., et al. 2006, *ApJ*, 651, 120
- Chabrier, G. 2003, *PASP*, 115, 763
- Chisholm, J., Tremonti, C. A., Leitherer, C., Chen, Y., & Wofford, A. 2016, *ArXiv e-prints*, arXiv:1601.05090
- Coil, A. L., Weiner, B. J., Holz, D. E., et al. 2011, *ApJ*, 743, 46
- Dean, C. A., & Bruhweiler, F. C. 1985, *ApJS*, 57, 133
- Elbaz, D., Daddi, E., Le Borgne, D., et al. 2007, *A&A*, 468, 33
- Erb, D. K., Quider, A. M., Henry, A. L., & Martin, C. L. 2012, *ApJ*, 759, 26
- Erb, D. K., Shapley, A. E., Pettini, M., et al. 2006, *ApJ*, 644, 813
- Faber, S. M., Willmer, C. N. A., Wolf, C., et al. 2007, *ApJ*, 665, 265
- Grimes, J. P., Heckman, T., Aloisi, A., et al. 2009, *ApJS*, 181, 272
- Heckman, T. M., Armus, L., & Miley, G. K. 1990, *ApJS*, 74, 833
- Heckman, T. M., Lehnert, M. D., Strickland, D. K., & Armus, L. 2000, *ApJS*, 129, 493
- Heckman, T. M., Sembach, K. R., Meurer, G. R., et al. 2001, *ApJ*, 554, 1021
- Kashino, D., Silverman, J. D., Rodighiero, G., et al. 2013, *ApJ*, 777, L8
- Kornei, K. A., Shapley, A. E., Martin, C. L., et al. 2012, *ApJ*, 758, 135
- . 2013, *ApJ*, 774, 50
- Lehner, N., Zech, W. F., Howk, J. C., & Savage, B. D. 2011, *ApJ*, 727, 46
- Leitherer, C., Ortiz Otálvaro, P. A., Bresolin, F., et al. 2010, *ApJS*, 189, 309
- Liang, C. J., & Chen, H.-W. 2014, *MNRAS*, 445, 2061
- Liang, C. J., Kravtsov, A. V., & Agertz, O. 2015, *ArXiv e-prints*, arXiv:1507.07002
- Markwardt, C. B. 2009, in *Astronomical Society of the Pacific Conference Series*, Vol. 411, *Astronomical Data Analysis Software and Systems XVIII*, ed. D. A. Bohlender, D. Durand, & P. Dowler, 251
- Martin, C. L. 1999, *ApJ*, 513, 156
- . 2005, *ApJ*, 621, 227
- Martin, C. L., & Bouché, N. 2009, *ApJ*, 703, 1394
- Martin, C. L., Shapley, A. E., Coil, A. L., et al. 2012, *ApJ*, 760, 127
- Murray, N., Quataert, E., & Thompson, T. A. 2005, *ApJ*, 618, 569
- Newman, J. A., Cooper, M. C., Davis, M., et al. 2013, *ApJS*, 208, 5
- Noeske, K. G., Weiner, B. J., Faber, S. M., et al. 2007, *ApJ*, 660, L43
- Oke, J. B., Cohen, J. G., Carr, M., et al. 1995, *PASP*, 107, 375
- Papovich, C., Dickinson, M., & Ferguson, H. C. 2001, *ApJ*, 559, 620
- Pettini, M., Rix, S. A., Steidel, C. C., et al. 2002, *ApJ*, 569, 742
- Pettini, M., Shapley, A. E., Steidel, C. C., et al. 2001, *ApJ*, 554, 981
- Prochaska, J. X., Kasen, D., & Rubin, K. 2011, *ApJ*, 734, 24
- Rix, S. A., Pettini, M., Leitherer, C., et al. 2004, *ApJ*, 615, 98
- Rubin, K. H. R., Prochaska, J. X., Koo, D. C., et al. 2014, *ApJ*, 794, 156
- Rupke, D. S., Veilleux, S., & Sanders, D. B. 2005, *ApJS*, 160, 115
- Salim, S., Rich, R. M., Charlot, S., et al. 2007, *ApJS*, 173, 267
- Salpeter, E. E. 1955, *ApJ*, 121, 161
- Schwartz, C. M., & Martin, C. L. 2004, *ApJ*, 610, 201
- Schwartz, C. M., Martin, C. L., Chandar, R., et al. 2006, *ApJ*, 646, 858
- Seibert, M., Martin, D. C., Heckman, T. M., et al. 2005, *ApJ*, 619, L55
- Shapley, A. E., Steidel, C. C., Pettini, M., & Adelberger, K. L. 2003, *ApJ*, 588, 65
- Shen, S., Madau, P., Guedes, J., et al. 2013, *ApJ*, 765, 89
- Steidel, C. C., Erb, D. K., Shapley, A. E., et al. 2010, *ApJ*, 717, 289
- Steidel, C. C., Shapley, A. E., Pettini, M., et al. 2004, *ApJ*, 604, 534
- Weiner, B. J., Coil, A. L., Prochaska, J. X., et al. 2009, *ApJ*, 692, 187
- Whitaker, K. E., Franx, M., Leja, J., et al. 2014, *ApJ*, 795, 104
- Willmer, C. N. A., Faber, S. M., Koo, D. C., et al. 2006, *ApJ*, 647, 853
- Wolfe, A. M., & Prochaska, J. X. 2000, *ApJ*, 545, 591

TABLE 1
GALAXY PROPERTIES AND VELOCITY MEASUREMENTS OF 93 OBJECTS WITH
C IV COVERAGE.

ID	Redshift	M_B (mag)	$U-B$ (mag)	$\log(M_*)$ (M_\odot)	A_{UV} (mag)	SFR_{UV} ($M_\odot \text{yr}^{-1}$)	$V_{C\text{ IV},1;1}$ (km s^{-1})	$V_{\text{Al II}}$ (km s^{-1})	$V_{\text{Si II}}$ (km s^{-1})	$V_{\text{nuvFe II}}$ (km s^{-1})
12008166	1.2854	-19.69	0.32	9.78	-86±54
12008445	1.2774	-20.69	0.52	10.22	-3±217	67±58	...	-76±40
12008509	1.2158	-19.80	0.36	9.76	-362±120
12008550	1.3025	-21.23	0.62	10.08	3.65	24	-205±39	-86±40	-187±35	-146±29
12008811	1.2156	-20.80	0.68	10.16	1.97	9	13±121	119±32	90±51	31±22
12011428	1.2841	-19.88	0.18	9.66	2.00	9	...	194±55
12011493	1.2638	-20.74	0.62	10.22	2.49	11	191±148	548±77	...	-2±41
12011619	1.0745	-19.31	0.44	9.11	0.05	2
12011742	1.3358	-20.81	0.71	10.23	-32±91	123±63	...	11±24
12011767	1.2817	-22.19	0.75	11.07	6.25	76	-298±161	-46±34
12012764	1.2353	-20.26	0.62	9.80	-466±124	-69±51
12012777	1.2743	-21.07	0.52	10.11	3.37	22	-287±40	-270±26	-156±45	-171±22
12012817	1.2158	-20.92	0.89	10.85	28±44
12012842	1.3148	-21.68	0.75	11.09	-398±87	-24±56	170±78	27±35
12012871	1.3443	-20.75	0.56	10.01	3.20	14	-52±88	-37±53	-10±142	-5±38
12013002	1.2184	-20.23	0.65	9.56	0.72	4	1±49
12013145	1.3406	-19.67	0.27	9.52	1.67	6	59±92	...
12013242	1.2868	-21.32	0.45	10.19	2.84	25	-180±48	-8±28	34±85	-79±19
12015563	1.2824	-21.30	0.60	10.35
12015682	1.2837	-21.53	0.62	11.20	3.25	27	...	-186±60
12015775	1.2243	-19.36	0.23	9.65	1.82	4	...	-218±177	...	-70±90
12015792	1.2307	-21.24	0.96	11.07	5.09	12
12015858	1.2307	-19.87	0.22	9.56	1.98	8	75±178	...	320±155	-30±59
12015914	1.1046	-19.83	0.33	10.11	2.60	8	121±179	148±62	113±116	68±25
12015933	1.2851	-20.35	0.66	9.70
12016019	1.0847	-20.72	0.62	10.03	4.52	18	...	69±108	...	47±17
12016075	1.1174	-19.68	0.54	9.41	2.88	5	18±53
12016903	1.1600	-21.46	0.51	10.21	2.35	25	135±29	61±46	...	4±36
12019542	1.2785	-21.68	0.71	10.40	5.41	40
12019996	1.2813	-21.71	0.63	10.67	4.32	43	316±159	52±68	...	121±28
12020064	1.3148	-21.12	0.60	10.35	4.71	26	...	-136±58
12024014	1.2977	-20.51	0.50	9.91
12024133	1.1241	-21.14	0.81	10.56	7.01	36	-45±24
12024181	1.0869	-21.00	0.80	10.54	7.63	35
12100420	1.1995	-20.63	0.60	10.02	2.35	9	-2±94	127±69	114±59	68±18
22004858	1.2687	-21.85	0.62	10.54	-64±79	199±29	112±42	82±15
22005523	1.2188	-21.68	0.61	10.41	94±69	...	-26±26
22005715	1.2345	-20.28	0.52	9.75
22006207	1.2709	-20.60	0.42	9.89	-472±60	-285±46
22012180	1.2894	-19.91	0.46	9.63
22012285	1.1700	-20.05	0.54	9.75	1162±68	143±111	...	33±33
22012322	1.1941	-20.42	0.57	9.84	214±114	...	-144±55
22012678	1.1959	-21.86	0.60	10.93	82±109	...	148±57
22013029	1.2710	-21.00	0.69	10.32	-658±92
22013827	1.2378	-21.25	0.75	10.52
22013864	1.2283	-21.00	0.72	10.38	-115±94	...	-99±28
22020736	1.1236	-21.83	0.99	10.99	-41±88
22036666	1.3468	-20.96	0.53	10.23
22036984	1.0804	-20.79	0.70	10.19
22044809	1.1869	-19.59	0.31	9.39
22100920	1.2735	-21.12	0.57	10.25	-18±29	...	-32±17
32016683	1.3006	-21.22	0.58	10.42	-114±44	22±28	14±69	-6±20
32017188	1.2526	-20.83	0.58	9.98
32019848	1.3433	-21.14	0.60	10.46
32019861	1.3077	-20.54	0.53	10.01
32019900	1.2478	-20.83	0.65	9.75
32019980	1.3487	-19.92	0.43	9.73	127±54	...
32020062	1.2808	-20.32	0.59	9.86	-244±92	-41±49
32020258	1.2461	-20.58	0.66	10.10
32020274	1.2589	-20.85	0.72	10.19	-78±69
32020317	1.1871	-20.28	0.47	9.72	-220±142	284±178	...	8±48
32020384	1.2493	-20.82	0.42	9.96	51±51	157±102	-33±29
32020441	1.0451	-20.51	0.61	10.04	254±100	...	-42±35
32020468	1.2355	-21.00	0.73	10.28
32020670	1.2330	-21.39	0.90	10.49
32020728	1.0446	-19.95	0.47	9.76	-27±39
32020769	1.3144	-20.77	0.41	10.01	-11±104	1±75	15±42
32020873	1.2491	-20.49	0.59	9.77	-112±40
42006781	1.2860	-20.74	0.55	9.69	-216±41	-153±22	-175±29	-70±15
42006799	1.2021	-21.74	0.91	11.26	-7±30
42006898	1.2410	-20.06	0.57	10.01	-300±168	...	38±38
42006904	1.0228	-20.74	0.46	10.07	-78±46

TABLE 1
GALAXY PROPERTIES AND VELOCITY MEASUREMENTS OF 93 OBJECTS WITH
C IV COVERAGE.

42014585	1.2706	-20.91	0.59	10.18	-143±95	-76±49	30±97	-152±38
42014618	1.0131	-20.38	0.59	9.81	-150±84	...	-71±15
42014718	1.1904	-21.27	0.69	10.86	4±122	-119±194	...	-141±27
42014758	1.2702	-21.82	0.65	10.67	-184±93	-98±49	-126±62	-32±20
42018218	1.2253	-20.15	0.50	9.79	142±58
42021285	1.1082	-20.65	0.71	10.17	-35±28
42022173	1.3112	-20.25	0.32	9.68	607±147	-338±58	176±133	-158±30
42022307	1.2595	-21.44	0.47	10.22	-292±63	-78±28	-32±36	-136±13
42025506	1.3358	-21.10	0.54	10.17	-10±84	-32±77	1±66	...
42025525	1.2946	-20.12	0.49	9.61
42025744	1.2024	-20.18	0.65	9.69
42025804	1.2435	-20.35	0.50	9.93
42026237	1.3385	-21.50	0.65	10.61
42026243	1.3457	-21.66	0.67	10.88	-193±102	...	-309±52
42026308	1.1700	-20.19	0.48	10.08
42026327	1.3461	-20.63	0.45	10.20
42026601	1.2272	-20.02	0.34	9.64
42033338	1.2237	-19.65	0.43	9.74
42034098	1.3465	-21.25	0.44	10.51	0±72	...	0±55
42034156	1.3464	-20.69	0.37	10.10	179±99	...	91±120	-35±33
42034223	1.2000	-20.09	0.44	9.45	-57±91	...	8±35

NOTE — Redshifts are from the DEEP2 catalog. The B -band luminosity and $U-B$ color are values taken from Willmer et al. (2006). M_* was estimated from SED fitting with *BRIK* photometry, as described in Bundy et al. (2006). A_{UV} is the extinction in the UV, which was used to derive SFR_{UV} , the dust-corrected SFR from GALEX measurements (full description in Section 2). Column 8-11 are velocity shifts measured from objects with continuum $S/N > 5$ and a line detection greater than 3σ (in terms of EW) using simple Gaussian fits. The listed line S/N was calculated by combining the doublet members for C IV, and Fe II $\lambda 2344$, $\lambda 2374$ and $\lambda 2587$ for the near-UV Fe II.